Flexible Optoelectronic Biointerfaces with Pseudocapacitive MnO_2 Nanostructures for Efficient Photostimulation of Neurons

by

Lokman Kaya

A Thesis Submitted to the
Graduate School of Sciences and Engineering
in Partial Fulfillment of the Requirements for
the Degree of

Master of Science

in

Electrical and Electronics Engineering

KOÇ
ÜNİVERSİTESİ

July 13, 2023

Flexible Optoelectronic Biointerfaces with Pseudocapacitive MnO_2 Nanostructures for Efficient Photostimulation of Neurons

Koç University

Graduate School of Sciences and Engineering

This is to certify that I have examined this copy of a master's thesis by

Lokman Kaya

and have found that it is complete and satisfactory in all respects,

and that any and all revisions required by the final

examining committee have been made.

Committee Members:

Assoc. Prof. Sedat Nizamoğlu (Advisor)

Prof. Ali Yapar

Assist. Prof. Aşkın Kocabaş

Date: 13/07/2023

[To Amida…]

ABSTRACT

Flexible Optoelectronic Biointerfaces with Pseudocapacitive MnO_2 Nanostructures for Efficient Photostimulation of Neurons

Lokman Kaya

Master of Science in Electrical and Electronics Engineering

July 13, 2023

This thesis explores the integration of flexible optoelectronic biointerfaces with 3D manganese dioxide (MnO_2) nanoflowers to achieve safe and efficient photostimulation of neurons. Optoelectronic biointerfaces have attracted significant attention for their potential in the wireless and electrical control of neurons. By utilizing 3D pseudocapacitive nanomaterials with interconnected porous structures and large surface areas, these biointerfaces can effectively transduce light into ionic currents, meeting the requirement for high electrode-electrolyte capacitance. The MnO_2 nanoflowers were grown through a chemical bath deposition technique on the return electrode, which was pre-coated with a MnO_2 seed layer deposited via cyclic voltammetry. The nanoflower integrated biointerfaces exhibited excellent performance with a high interfacial capacitance (greater than 10 mF cm^{-2}) and photogenerated charge density (over 20 μC cm^{-2}) even under low light intensity conditions (1 mW mm^{-2}). Importantly, the MnO_2 nanoflowers induced safe capacitive currents through reversible Faradaic reactions and demonstrated no toxic effects on hippocampal neurons during in vitro experiments, making them a promising material for curvature fit integration with electrogenic cells. The functionality of the optoelectronic biointerfaces was assessed using a patch-clamp electrophysiology setup in the whole-cell configuration of hippocampal neurons, revealing their ability to elicit repetitive and rapid firing of action potentials in response to light pulse trains. This research underscores the potential of electrochemically-deposited 3D pseudocapacitive nanomaterials as a robust and efficient approach for controlling neurons through optoelectronic means.

ÖZETÇE

Pseudokapasitif MnO_2 Nanoyapılarına Sahip Esnek Optoelektronik Biyoarayüzlerin Etkili Nöron Fotostimülasyonu İçin Kullanımı

Lokman Kaya

Elektrik ve Elektronik Mühendisliği, Yüksek Lisans

13 Temmuz 2023

Bu tez, esnek optoelektronik biyoarayüzlerin güvenli ve verimli bir şekilde sinir hücrelerinin fotostimülasyonu için 3 boyutlu mangan dioksit (MnO_2) nanoçiçeklerle entegrasyonunu araştırmaktadır. Optoelektronik biyoarayüzler, kablosuz ve elektriksel olarak sinir hücrelerinin kontrolü için önemli bir ilgi uyandırmaktadır. Porlu yapıya ve geniş yüzey alanına sahip 3 boyutlu psödokapasitif nanomalzemeler kullanarak, bu biyoarayüzler ışığı iyonik akımlara etkin bir şekilde dönüştürebilme özelliğine sahiptir ve yüksek elektrot-elektrolit kapasitesi gereksinimini karşılayabilmektedir. MnO_2 nanoçiçekler, kimyasal banyo çöktürme yöntemiyle geri dönüş elektrodu üzerinde büyütülmüş olup, MnO_2 tohum tabakası da döngüsel voltametri kullanılarak önceden kaplanmıştır. Nanoçiçekler düşük ışık yoğunluğu koşullarında bile (1 mW mm^{-2}), yüksek bir arayüzey kapasitansı (10 mF cm^{-2}'den büyük) ve fotogeneratik yük yoğunluğu (20 µC cm^{-2}'den fazla) sergilemiştir. MnO_2 nanoçiçekler, tersinir Faraday reaksiyonları aracılığıyla güvenli kapasitif akımlar oluşturmuş ve in vitro deneylerde hipokampal sinir hücreleri üzerinde herhangi bir toksisiteye neden olmamıştır, bu da elektrojenik hücrelerle entegrasyon için umut verici bir malzeme olduğunu göstermektedir. Optoelektronik biyoarayüzlerin işlevselliği, hipokampal sinir hücrelerinin tüm hücre yapılandırmasıyla yama kelepçesi elektrofizyolojisi kullanılarak değerlendirilmiş ve periyodik ışık atımlarına yanıt olarak tekrarlayan ve hızlı bir şekilde aksiyon potansiyellerinin tetiklenmesini ortaya koymuştur. Bu araştırma, elektrokimyasal olarak çöktürülen 3 boyutlu psödokapasitif nanomalzemelerin sinir hücrelerini optoelektronik yollarla etkili bir şekilde kontrol etmek için sağlam ve verimli bir yaklaşım olarak potansiyelini göstermiştir.

ACKNOWLEDGMENTS

The author expresses gratitude to Assoc. Prof. Sedat Nizamoğlu for his support before, after, and during this journey, as well as IDEALAB's former and current members.

The author expresses gratitude to the thesis committee, Assist. Prof. Aşkın Kocabaş, Prof. Ali Yapar and Assoc. Prof. Sedat Nizamoğlu for their valuable time and input.

The author thanks the family members for their continuous support and faith.

The author expresses gratitude to Koc University Surface Science and Technology Center (KUYTAM) for providing the scanning electron microscopy images. Additionally, the authors acknowledge the utilization of services and resources provided by Koç University Research Center for Translational Medicine (KUTTAM), which is funded by the Republic of Turkey Ministry of Development. However, the responsibility of the content solely belongs to the authors, and it may not necessarily reflect the official perspectives of the Ministry of Development. The author acknowledges funding from the European Union (ERC, MESHOPTO, 101045289). Views and opinions expressed are, however, those of the author only and do not necessarily reflect those of the European Union or the European Research Council Executive Agency. Neither the European Union nor the granting authority can be held responsible for them. The author also acknowledges the Scientific and Technological Research Council of Turkey (TUBITAK) with Project Nos. 121C301, 120E329, and 121E376.

TABLE OF CONTENTS

LIST OF TABLES

LIST OF FIGURES

ABBREVIATIONS

NF	Nanoflowers
AP	Action Potential
BI	Biointerface
SEM	Scanning Electron Microscopy
ITO	Indium Tin Oxide
FESEM	Field Emission Scanning Electron Microscopy
DBS	Deep Brain Stimulation
PEDOT:PSS	poly(3,4-ethylenedioxythiophene):poly(styrenesulfonate)
MnO_2	Manganese Dioxide
RuO_2	Ruthenium Dioxide
WPP	Working Potential Window
Co_3O_4	Cobalt Oxide
ZnO	Zinc Oxide
$Ni(OH)_2$	Nickel Hydroxide
CuO	Copper Oxide

Chapter 1:
INTRODUCTION

Cell stimulation is a fundamental mechanism that enables vital functions in living organisms, ranging from sensory perception to regulating physiological processes through the secretion of hormones and enzymes [1]. Studying biomolecular dynamics within cells and treating neurological disorders such as paralysis, epilepsy, and Parkinson's disease, often require artificial cellular stimulation [2, 3]. Light-based stimulation has emerged as a non-invasive, localized, and wireless method for achieving cell stimulation, utilizing near-infrared light, optogenetics, and optoelectronic neural interfaces[4-6]. These interfaces have gained significant attention due to their non-genetic nature and reduced interference with cellular integrity, making them particularly suitable for neuroscience experiments.

Capacitive charge injection mechanisms play a crucial role in artificial cellular stimulation studies. Ions are cumulated in the electrolyte/electrode interface to generate stimulating potential fields near the cell membrane, relying on electrochemical gradients [7]. The capacitive mechanism is a rapid and safe charge-injection mechanism for neural stimulation due to its suppressed redox reactions and minimized heating effects, making them suitable for minimally invasive neural stimulation. Previous studies have utilized organic pigments, pi-conjugated polymers, p-n semiconducting organic nanocrystals, and quantum dot-integrated organic polymers to generate capacitive photocurrents in biointerfaces [8-10]. However, enhancing the double-layer capacitance to achieve the threshold charge injection for neural stimulation remains a significant challenge [11].

To overcome this challenge, the adaptation of supercapacitor technology to organic biointerfaces has emerged as a promising approach. Supercapacitors introduce pseudocapacitance, which is based on fast and reversible redox reactions, in addition to the double-layer capacitance [12]. Pseudocapacitance can significantly increase the total interfacial capacitance, offering a higher charge storage capacity compared to the double-layer capacitance alone [13]. Organic polymers, acting as electron and hole transport layers as well as the photoactive material, can be combined with semiconductor

nanocrystals and hydrogels to develop efficient and safe photovoltaic biointerfaces for cellular stimulation [6].

The primary objective of this thesis is to explore the potential of 3D supercapacitors in photovoltaic biointerfaces for neural stimulation. This research investigates the utilization of supercapacitor technology to enhance the charge injection capabilities of organic biointerfaces, particularly in terms of achieving threshold charge injection for neural stimulation. The organization of the thesis is as follows: Chapter 1 introduces neural interfaces, emphasizing their significance for stimulation purposes. Chapter 2 presents a general background for neural stimulation types and charge injection mechanisms. Chapter 3 focuses on the study of pseudocapacitive biointerfaces and their results and performances. Finally, Chapter 4 concludes the thesis and outlines future directions for research in the field of optoelectronic neural interfaces.

Chapter 2:
BACKGROUND

In this chapter, we present a general background about neural stimulation types and the advantages of optoelectronic stimulation.

2.1 Neural Stimulation and Bioelectronic Medicine

Neural stimulation plays a significant role in the field of bioelectronic medicine. It offers promising approaches for treating various neurological disorders, such as paralysis, Parkinson's disease, and epilepsy [2, 3]. The primary mechanism behind neural stimulation can be summarized as the application of electrical currents to modulate the activity of neurons. These currents are generated by the flow of mainly sodium (Na^+) and potassium (K^+) ions due to the potential differences between active and return electrodes [14]. Direct electrical stimulation via leads has been the primary method for controlling neural activity. However, the need for wireless and less invasive alternatives for electrical stimulation has been addressed [15]. Even though applying an electrical pulse directly is very effective and straightforward, this method has certain limitations and drawbacks. One of the drawbacks is that the direct application of electrical potential can be invasive, requiring surgical procedures to implant leads into specific nervous system regions. Moreover, precise targeting and particular types of modulation of neural circuits may pose challenges with conventional direct stimulation techniques.

In recent years, luckily, optoelectronic neural interfaces have emerged as a promising approach for wireless and precise modulation of neural activity [16, 17]. Light-based stimulation provides a minimally invasive method with exceptional temporal and spatial resolution. The working mechanism of the photoelectrode can be explained simply in a few steps. The light absorbed by the photodiode creates electron-hole pair due to the absorbed photon. The photogenerated charge carriers then move generally in opposite directions due to different energy levels of the device layers, which, in turn, induce an electrical potential difference in the cellular environment. This optoelectronic approach enables precise and localized stimulation of neurons, opening new roads for neural control. For instance, in the treatment of blindness caused by macular degeneration, rigid photovoltaic devices made of silicon have been utilized to stimulate secondary neurons

in the retina, leading to partial recovery of sight [18]. However, the limitations of rigid devices present a drawback. The development of flexible optoelectronic neural interfaces is crucial to allow better conformability to the complex shapes and structures of neural tissues, reducing the risk of tissue damage and enhancing the interfaces' long-term biocompatibility [19].

2.2 Optoelectronic Neural Interfaces

Optoelectronic neural interfaces are promising alternatives to traditional electrical stimulation methods. They offer various advantages, such as precision, spatial resolution, and non-invasiveness [17, 20]. Thanks to the high spatial resolution of light, we can both stimulate and silence specific neurons depending on the application. The multiwavelength property of light also paves the way for selective and multi-channel stimulation scenarios. The activation and inhibition possibility enables us to study and treat patients with sight loss or neurological disorders like epilepsy. The ability to selectively stimulate or silence neurons using different wavelengths of light allows finer control over neural activity in a neural network [21]. At the same time, the non-invasive nature of light-based stimulation decreases tissue damage and immune responses [21].

Optoelectronic neural interfaces hold promise for treating various neurological disorders in clinical applications. For example, they have been used to restore vision by stimulating retinal neurons with silicon-based biointerfaces [18]. Optoelectronic interfaces have also shown potential in deep brain stimulation (DBS); compared to traditional electrical stimulation by leads, it offers a more targeted and adaptable approach [22]. These interfaces enable high-resolution spatial and temporal control over neural circuits by utilizing photodiodes, light sources, and signal processing units. Advancements in optoelectronic interfaces opened new roads for clinical applications in treating neurological disorders, and it holds tremendous potential for advancing our understanding of the brain and developing new therapeutic strategies.

2.3 Flexible Optoelectronic Neural Biointerfaces

The advancement in the field of bioelectronics offers several advantages over conventional rigid devices, such as improved biocompatibility, reduced risk of tissue damage, and better conformability to neural tissues [23, 24]. However, designing flexible optoelectronic neural interfaces comes with its own set of challenges, as most of the flexible and biocompatible materials are organic matters. One of the considerations is the selection of photoactive materials for appropriate device architecture in terms of energy band levels. Another consideration is the sufficient absorption of light. The correct choice of photoactive material is essential for efficiently converting light into photogenerated charge carriers, which induce electrical potential differences in the cellular environment. The device thickness should not exceed a few microns to ensure flexible, tissue-compatible, thin devices [25]. However, absorbing a sufficient amount of light is also required, which is correlated with photoactive layer thickness. Thus, another consideration is the absorption coefficient of the photoactive organic material. High absorption coefficients ensure the device can operate under low light intensities, reducing potential phototoxicity while achieving effective neural stimulation.

Flexible optoelectronic neural interfaces need to be capable of injecting sufficiently high ionic charge levels. Traditional approaches based on double-layer capacitance have limitations in achieving high charge injection levels due to fast spikes induced by the capacitance [26]. As a result, alternative methods utilizing planar PEDOT:PSS, TiN, and RuO_2 have been explored to increase charge injection levels due to their high capacitance [27-29]. However, these methods may still fail to achieve the desired charge levels.

A promising approach to enhance charge injection is to use 3D pseudocapacitive nanostructures. These supercapacitive nanostructures offer increased electrode-electrolyte interactions, higher charge storage capacities, and charge injection levels due to their higher surface area [30]. Among the various 3D pseudocapacitive materials, like cobalt oxide (Co_3O_4)[31], nickel hydroxide ($Ni(OH)_2$) [32], zinc oxide (ZnO)[33], copper oxide (CuO)[34], and ruthenium oxide (RuO_2) [35], MnO_2 nanoflowers (NFs) have attracted significant attention for their unique properties, such as high capacitance per unit mass, wide operational potentials, low toxicity, and abundant availability [36-41]. Biocompatibility is crucial when developing neural interfaces, as it ensures the long-term

viability and functionality of the implanted devices within the biological system. Thus, integrating MnO_2 NFs into flexible optoelectronic neural interfaces can provide an effective and safe charge injection for neural stimulation.

2.4 Charge Injection Mechanisms for Neural Interfaces and Pseudocapacitance

There are mainly three kinds of charge injection mechanisms: capacitive, faradaic, and pseudocapacitive. In this study, we use a pseudocapacitive material due to several advantages, such as reversible reactions and high and safe charge injection. In the following subsection, three mechanisms are explained in more detail.

2.4.1 Faradaic Charge Injection

Faradaic charge injection involves the transfer of charge through electrochemical reactions at the interface between the electrode and the surrounding electrolyte. This mechanism enables efficient charge transfer, which is desirable for neural stimulation. However, the reactions should be reversible, and biphasic stimulation should be used, meaning the net charge should be zero. In most cases, either biphasic stimulation is not possible, or irreversible redox reactions occur. This makes the faradaic charge injection mechanism partially safe and, most of the time, toxic to the tissue. Only if we minimize undesired side reactions and heating effects associated with faradaic charge injection, we may ensure safe and controlled stimulation.

2.4.2 Capacitive Charge Injection

Capacitive charge injection operates by modulating the electrical double layer formed at the electrode-electrolyte interface. By applying an external voltage, the electrical double layer is altered, resulting in the accumulation or depletion of charge near the electrode surface. This charge modulation generates potential fields that can stimulate nearby cells or neurons. We also observe the inner and outer Helmholtz planes in this mechanism. Capacitive charge injection offers a rapid and safe stimulation method, as it avoids faradaic reactions and their associated side effects. It is widely considered the preferred approach for minimally invasive neural stimulation due to its low power

requirements and reduced heat generation. However, due to the limited charge injection capacity, organic polymer-based optoelectronic biointerfaces may fail to stimulate neurons to induce action potentials [21].

2.4.3 Pseudocapacitive Charge Injection and Nanostructures

Pseudocapacitive charge injection combines features of both capacitive and faradaic charge injection mechanisms. It involves fast and reversible redox reactions at the electrode-electrolyte interface, like faradaic charge injection. However, unlike faradaic reactions, pseudocapacitive reactions do not include the formation of chemical bonds or significant changes in the electrolyte composition like pH [42]. In short, pseudocapacitance refers to the ability of certain materials to store and release charge at the electrode-electrolyte interface through reversible redox reactions or ion intercalation processes. Unlike conventional capacitors, which rely on only double-layer capacitance, pseudocapacitive materials offer higher charge storage capacity. This property makes them well-suited for neural interfaces as it enables more efficient charge injection, improving stimulation efficiency and control over neural activity.

Pseudocapacitive materials possess several advantageous properties that make them attractive for integration into neural interfaces. They exhibit high capacitance per unit area or mass, allowing for efficient charge storage and delivery. This increased capacitance enables the injection of more significant amounts of charge, facilitating the effective stimulation of neurons. Additionally, pseudocapacitive materials have a wide potential range, making them suitable for various applications requiring different operation potential windows. Another important aspect is the compatibility of pseudocapacitive materials with biological systems, and these materials can be engineered to have biocompatible surfaces, minimizing adverse reactions and ensuring long-term stability when interfacing with neural tissue. They also promote efficient charge transfer and minimize impedance at the electrode-electrolyte interface, facilitating effective communication with neural cells.

Specific pseudocapacitive materials have been explored and successfully integrated with the context of neural interfaces to enhance charge injection levels and

biocompatibility. One example is conducting polymer-based pseudocapacitive electrode poly(3,4-ethylenedioxythiophene):poly(styrenesulfonate) (PEDOT:PSS) which has shown promising results in improving electrical stimulation efficiency and promoting neural cell adhesion, making them favorable for neural interfacing applications [6]. Another example is RuO_2; previous reports show that it can enhance injected charge for neurostimulation [43]. However, the porous structure of RuO_2 can only provide a limited surface area. To achieve more charge storage in pseudocapacitive materials, the surface area must be increased since all the reaction takes place on the surface of the material. One example is MnO_2 nanoflowers, which exhibit high pseudocapacitance due to their reversible redox reactions, and they have been effectively used in flexible optoelectronic biointerfaces for stimulating neurons [21]. These nanoflowers offer a high interfacial capacitance and low impedance enabling efficient charge storage and delivery while maintaining compatibility with neuronal cells.

Integrating pseudocapacitive materials, including RuO_2, MnO_2 nanoflowers, and PEDOT:PSS, into neural interfaces, represents significant progress in improving charge injection levels and biocompatibility. These advancements pave the way for more efficient and precise stimulation techniques, contributing to the development of advanced bioelectronic medicine for neurological disorders.

2.5 Motivation and Objectives of the Study

The motivation behind this research project stems from the need to advance the field of neural interfaces and overcome existing limitations in stimulation techniques. While optoelectronic neural interfaces have shown promise in wireless and less invasive electrical stimulation, there is a need to develop flexible interfaces with improved charge injection capabilities. Current methods face challenges in achieving high charge levels and maintaining biocompatibility; therefore, this study aims to address these limitations and contribute to the development of flexible optoelectronic neural interfaces that offer enhanced charge injection efficiency and biocompatibility.

The main focus is to explore the potential of integrating MnO_2 nanoflowers into a flexible optoelectronic biointerface for the photostimulation of neurons. The study aims to achieve several specific objectives. First, the goal is to fabricate a flexible optoelectronic biointerface incorporating MnO_2 nanoflowers using a simple and efficient manufacturing process. Next, the interfacial capacitance and photogenerated charge density of the MnO_2 nanoflowers will be characterized in a biological medium under low light-intensity conditions. The biocompatibility of the MnO_2 nanoflowers will also be evaluated, and patch-clamp electrophysiology will be conducted on hippocampal neurons to assess their response to photostimulation. Additionally, the performance of the flexible optoelectronic biointerface will be analyzed to determine its effectiveness in inducing the repetitive firing of neurons under illumination.

This study's contribution lies in exploring MnO_2 nanoflowers as pseudocapacitive nanostructures for flexible organic optoelectronic neural interfaces. By integrating these nanoflowers into the biointerface, we aim to improve charge injection levels and investigate their biocompatibility with neural cells. The study's novelty lies in using the 3D morphology of MnO_2 nanoflowers for optoelectronic biointerfaces for the first time. The findings from this research will provide insights into the potential of 3D pseudocapacitive materials for enhancing the functionality and safety of optoelectronic neural interfaces, contributing to the advancement of bioelectronic medicine for neurological disorders. In conclusion, this study aims to expand our understanding of flexible optoelectronic neural interfaces and pave the way for future developments in the field, ultimately benefiting patients with neurological disorders and advancing the field of bioelectronic medicine.

Chapter 3:

MNO_2 NANOFLOWER INTEGRATED OPTOELECTRONIC BIOINTERFACES FOR PHOTOSTIMULATION OF NEURONS

(This chapter is reprinted (adapted) with permission from Kaya, Lokman et al. (2023) MnO_2 Nanoflower Integrated Optoelectronic Biointerfaces for Photostimulation of Neurons. *Advanced Science*: 2301854. Copyright 2023. Wiley Online Library)

3.1 Introduction

Bioelectronic medicine uses electrical signals to stimulate or silence neurons to treat various neurological diseases, such as paralysis, Parkinson's disease, and epilepsy [44]. Fundamentally electrical currents in the body are generated by the flow of the ions such as sodium (Na^+) and potassium (K^+) because of the induced potential differences between the active and return electrodes [45, 46]. Although the conventional way to control neural activity is to apply electrical potentials by leads directly, there is an active search for wireless and less invasive electrical stimulation alternatives [47-50]. Light provides a noninvasive and spectrally multiplexable trigger option with exceptional temporal and spatial resolution. Moreover, light can be absorbed by photodiodes, create photogenerated charge carriers and induce an electrical potential difference in cellular environments via optoelectronic neural interfaces for the photostimulation of neurons.

Optoelectronic neural interfaces have drawn significant attention for wireless modulation of various tissues, such as the heart, brain, and peripheral nerves [23, 50, 51]. Even in the clinics, they have already started to show vital benefits against blindness caused by macular degeneration, and the 30 Hz rate photostimulation of secondary neurons in the retina led to the partial recovery of sight [52]. For that, rigid photovoltaic devices made of silicon were beneficially used. One of the challenges is to develop flexible optoelectronic neural interfaces that can effectively inject high ionic charge levels via a capacitive charge injection mechanism. Since the bending stiffness is proportional to the cube of the thickness, using photoactive materials with a high absorption coefficient is critical for fabricating flexible devices [53]. So far, flexible optoelectronic neural interfaces have been realized via organic polymers, indigo dyes, and quantum dots [23, 29, 54, 55]. Even though they showed safe capacitive photocurrents, these devices fall short on the injected charge levels because of the double-layer capacitance-induced

spikes. To increase the charge injection levels, planar PEDOT:PSS, TiN and RuO_2 were used [10, 43, 56]. Alternatively, 3D pseudocapacitive nanostructures with enhanced electrode-electrolyte interactions has high potential for the neural interfaces.

In this study, we integrate MnO_2 nanoflowers (NFs) into a flexible optoelectronic biointerface for the photostimulation of neurons. A MnO_2 seed layer is initially formed via cyclic voltammetry, and then the nanoflowers are grown on the seed layer via chemical bath deposition. The nanoflower morphology resulted in a high interfacial capacitance larger than 10 mF cm^{-2} in a biological media and a high photogenerated charge density over 20 μC cm^{-2} under a low light intensity of 1 mW mm^{-2}. Besides the advantageous properties of MnO_2, such as high capacitance per unit mass [37, 38], wide operational potentials [41], and being an abundant raw material [39, 40], we observed that MnO_2 nanoflowers do not induce any toxicity on the hippocampal neurons. We did patch-clamp electrophysiology of hippocampal neurons on the biointerface under whole-cell recording, and we observed the repetitive firing of neurons under the illumination of pulse trains. Our study highlights the 3D nanomorphology of pseudocapacitive materials as a promising tool for the optoelectronic control of neurons.

3.2 Methods

In this chapter, we give details about experimental methods and the characterization devices used while obtaining the results presented in the following sections.

3.2.1 Device Fabrication

Photoelectrodes were fabricated on glass or PET substrates covered with indium tin oxide (ITO). The glass/ITO (Ossilla, S111) or PET/ITO (Sigma Aldrich, 639303) substrates were cleaned in an ultrasonic cleaner system at 50 °C with immersing consecutively in a sodium hydroxide (NaOH) solution for 5 min, tension-active agent (HELLMANEX III):deionized water (3%, 97% by volume) for 15 min, deionized water for 15 min (repeated two times to remove access HELLMANEX), acetone for 10 min, and isopropanol for 10 min. After oven drying at 60 °C for 30 min, the substrates were treated with UV ozone for 20 min to eliminate any other residues on the ITO surface. The ZnO precursor solution was prepared by mixing 110 mg of zinc acetate dehydrate ($Zn(CH_3CO_2)_2 \cdot 2H_2O$) (Sigma-Aldrich) in 1 mL of 2-methoxyethanol ($C_3H_8O_2$) and 42 mg

of ethanolamine ($HOCH_2CH_2NH_2$) and the mixture is stirred for 5 min. Then the ZnO solution was sonicated for 2 h at 50 °C and filtered through a 0.45 μm PVDF filter. The P3HT (95.7% regioregular, >99% pure, Ossilla) and PCBM (>99% pure, Ossilla) solutions were prepared by mixing the donor material (P3HT) and the acceptor material (PCBM) solutions with the blending ratio of 1:1. P3HT and PCBM solutions were prepared separately in o-dichlorobenzene with optimized concentrations of 60 mg mL^{-1} (Figure 3.2), stirred at 50 °C for 8 hours, and then mixed and stirred at 50 °C for 3 hours using a magnetic stirrer. The ZnO solution was spin-coated on ITO substrates at 2000 rpm for 60 seconds, and half of the substrate was cleaned by wiping with cotton swabs soaked with methanol. Then, the substrates were annealed at 280 °C for 15 min for glass/ITO substrates and 200 °C for 30 min for PET/ITO substrates. Later, The photoactive layer was fabricated by spin-coating the P3HT:PCBM blend onto the ZnO layer at 1000 rpm for 60 seconds, and half of the substrate was cleaned by wiping with cotton swabs soaked with toluene. Later, the devices were annealed at 150 °C for 10 min to form P3HT:PCBM bulk heterojunction. After these steps, the photoactive part of the neural interface is formed on one half of the device, while unmodified ITO is on the other half. To assemble the MnO_2 return anode electrode on the intact ITO region, first, the MnO_2 seed layer was electrodeposited by submerging the ITO return electrode region into $MnSO_4$:Na_2SO_4 (5mM:0.1M) aqueous solution at room temperature and performing CV measurement for 5 cycles with 10 mV s^{-1} sweep rate from 0.4 V to 1.3 V with respect to Ag/AgCl bath electrode [57]. The devices were rinsed in distilled water and annealed at 50 °C for 30 min. For gold substrates in this step, we needed to decrease the step rate to 4 mV s^{-1} and deposition cycle to 2 to get as gold is more conductive, and a lower step rate ensures the current is not overloaded and stays within a few mA range during CV coating. Similarly, for stainless steel mesh, we used 2 mV s^{-1} step voltage and 1 deposition cycle due to the high conductivity and high surface area of the substrate. For FTO substrates, due to higher impedance, we increased step voltage to 12 mV s^{-1} and deposition cycle to 6, while the annealing temperature was increased to 80 °C degree to ensure better attachment of the seed layer due to the higher thickness of FTO substrates. Then, to form a high-surface-area porous oxide layer for obtaining a large return electrode capacitance, the MnO_2 NFs layer was constructed on top of the MnO_2 seed layer by chemical bath deposition. In this technique, the MnO_2 seed layer was immersed into the highly concentrated Na_2SO_4:$MnSO_4$:$K_2S_2O_8$ (0.33M:0.33M:0.33M) aqueous solution

[58] for 2 hours at 60 °C to form nanoflowers on the return electrode region; then they are annealed at 70 °C for ITO substrates. Chemical bath deposition duration remained the same for all substrates with a slight alteration in bath temperature and annealing temperature to have similar morphologies and ensure nanoflower attachment (Table 3.2). These parameters can be adjusted for the targetted morphology and nanoflower shapes [58]. The MnO_2 nanoflowers fabricated on FTO, gold, and stainless steel substrates show similar morphologies compared to ITO substrates (Figure 3.13). Besides these substrates, MnO2 flowers can also be obtained on graphene, graphite, and zeolitic imidazolate framework [59-61].

3.2.2 X-ray photoelectron spectroscopy Analyses

A Thermo Scientific K-Alpha XPS conducted XPS analyses of MnO2 nanoflowers with Al K-alpha monochromatic radiation (1486.3 eV). Dried samples were exposed to 400 μm X-ray spot size and 50.0 eV pass energy for XPS measurements. The experimental and base pressures were kept below about 1×10^{-7} mbar and 3×10^{-9} mbar, respectively. The C 1s peak at 285.0 eV was designated for the assessment.

3.2.3 Photoelectrochemical Measurements

We used an Autolab Potentiostat Galvanostat PGSTAT system (Metrhom, Netherlands) for photoelectrochemical measurements, such as chronoamperometry, chronopotentiometry, cyclic voltammetry, and electrochemical impedance characterization. The three-electrode system was used with a platinum rod as the counter electrode, Ag/AgCl as the reference electrode, and a connection to the ITO layer of the BI as the working electrode. 1 cm^2 of the biointerface with the other two electrodes was immersed in an extracellular aCSF medium that mimics in vivo environment as an electrolyte solution at room temperature. The aCSF medium was prepared by mixing 10 mM of 4-(2-hydroxyethyl)-1-piperazineethanesulfonic acid (HEPES), 10 mM glucose, 2 mM $CaCl_2$, 140 mM of NaCl, 1 mM of $MgCl_2$, and 3 mM of KCl. The pH of aCSF solution was adjusted to 7.4 by adding the required amount of NaOH solution. Then, a blue LED (M450LP1, Thorlabs) was used as the light source. The LED was driven by an LED Driver with Pulse Modulation (DC2200-High-Power 1-Channel, Thorlabs) to produce a train of 20 ms light pulses. Then, the data was recorded and analyzed using the

NOVA software. An optical power meter (Newport 843-R) was utilized to measure the optical power densities of incident light on the biointerface.

3.2.4 Primary Neuron Isolation

The Institutional Animal Care has approved all experimental procedures and Use Committees of Koç University (Approval No: 2021.HADYEK.022) according to Directive 2010/63/EU of the European Parliament and of the Council on the Protection of Animals Used for Scientific Purposes. To isolate primary hippocampal neurons, the brains of Wistar Albino rats at embryonic day 15-17 (E15-E17) were dissected, and brains were cleared of blood vessels and the meninges. Then hippocampi were obtained and placed in ice-cold Hank's Balanced Salt Solution (HBSS, Thermo Fisher Scientific, MA, USA) supplemented with glucose and sucrose. The hippocampi were incubated in 0.25% Trypsin-EDTA solution (Thermo Fisher Scientific, MA, USA) supplemented with 2% DNase-I (NeoFroxx, Einhausen, Germany) for 20 minutes in a 37ºC incubator. After incubation, Dulbecco's Modified Eagle Medium/Nutrient Mixture F-12 (DMEM/F12 Thermo Fisher Scientific, MA, USA), including 10% fetal bovine serum (FBS, Heat Inactivated, GE Healthcare, IL, USA) and 1% penicillin/streptomycin (Thermo Fisher Scientific, MA, USA) was added to inhibit excess enzyme activity and tissue suspension was centrifuged. The supernatant was removed, and freshly prepared plating Neurobasal Medium (NBM, Thermo Fisher Scientific, MA, USA) including 2% B27, 1% L-glutamine, 1% penicillin/streptomycin, β-mercaptoethanol, glutamate was added to the pellet. The remaining tissue was mechanically dissociated by trituration with a Pasteur pipet, and cells were collected in a falcon tube after passing through a 70 µm cell strainer. The homogenous cell solution was seeded on poly-l-lysine (PLL, Sigma-Aldrich, MO, USA) coated ITO and MnO_2 substrates. Cells were incubated for 3 days at 37ºC incubator with 5% CO_2; then, the media was changed with NBM supplemented with cytosine arabinoside (Sigma-Aldrich, MO, USA) to eliminate glia proliferation. After glia removal, fresh NBM was replaced to maintain culturing until experiments.

3.2.5 Electrophysiology Experiments

The electrical activity of cultured hippocampal neurons was recorded by utilizing EPC 800 Heka Elektronik patch-clamp amplifier system (Pfalz, Germany). In the whole-

cell configuration, the voltage-clamp and current-clamp recordings were performed for single-cell transmembrane current and transmembrane voltage recordings, respectively. The recorded cells were on the photoactive region of the BI submerged in aCSF extracellular medium without any wire connection. The reference Ag/AgCl bath electrode was far from the BI to mimic in vivo conditions. The patch-pipettes with 6-8 MΩ resistance were prepared by filling them with intracellular medium, which consisted of 140 mM KCl, 2 mM MgCl2, 10 mM HEPES, 10 mM ethylene glycol-bis (β-aminoethyl ether)-N,N,N′,N′-tetraacetic acid (EGTA), 2 mM Mg-ATP, and a required amount of KOH to adjust the pH to 7.2, in distilled water. The current-clamp data was subjected to downsampling to reduce the computational complexity for statistical analysis of action potentials while preserving the integrity of the data (Figure 3.11). The goal was to conduct a meaningful analysis of the action potentials without sacrificing vital information. A digital camera integrated with an Olympus T2 upright microscope was used to observe the patch pipette and cells. Photocurrent analysis was conducted using the identical system with the patch-clamp amplifier in voltage-clamp mode, and the biointerface was not cultivated with cells yet. The pipette was 100 micrometers above the surface of the biointerface and had 4-6 MΩ resistance for the measurement.

3.2.6 Biocompatibility Assay

CellTiter-Glo Luminescent-based cell viability assay (CTG, Promega, Mannheim, Germany) was used to quantify alive cells on the control and MnO_2 biointerfaces. This technique provides quick results to detect the number of viable cells depending on the amount of ATP in cell populations. Isolated primary hippocampal neurons were seeded as 500000 cells/well on PLL-coated devices and cultured as explained above. To determine cell viability, a 1:1 ratio of CTG solution was added to cells and shaken for 2 minutes on an orbital shaker. Then cells were allowed 10 minutes of incubation at RT to stabilize luminescence signals. After incubation, the solution was transferred to a 96-well opaque plate, and the luminescence signals were measured with Synergy H1 Microplate Reader (Bio-Tek Instruments). The relative cell viability of each sample was calculated as follows: Viability = (ODsample/ODcontrol) × 100. The sample's optical density (OD) was obtained from the cells grown on the MnO_2 device, and the OD of the control was obtained from the cells grown on the ITO control substrates.

3.2.7 Immunofluorescence Staining and Imaging

Primary hippocampal neurons were seeded as explained above on the ITO control, and the MnO_2 substrates as 500000 cells/substrate. The short-term effect of substrates on cells was checked at Day 0, and long-term alteration in neuron characteristics and morphology was monitored on the 14th day of culture. The neurons at Day 0 or Day 14 were fixed by ice-cold 4% paraformaldehyde in PBS for 20 min and washed three times with PBS-T (Phosphate Buffered Saline, 0.1% Tween-20). For permeabilization, the cells were incubated with 0.1% TritonX-100 in PBS for 8 min. Then, they were incubated with Superblock (Thermo Fisher Scientific, MA, USA) for 10 min at room temperature. For neuron characterization, primary hippocampal neurons were incubated overnight with an anti-NeuN antibody (ab177487, Abcam, Cambridge, UK) prepared in a blocking solution. After incubation, samples were washed with PBS-T and incubated with goat anti-rabbit IgG H&L Alexa Fluor 488 (Cell Signaling Technology, MA, USA) to label anti-NeuN for 90 minutes at 37°C. To show the cytoskeleton of neurons grown on either the control substrate or MnO_2 device, cells were stained with FITC-conjugated phalloidin antibody for 90 minutes at 37°C. All samples were washed thrice with PBS-T, then mounted with DAPI-supplemented mounting medium (50001, Ibidi GmbH, Germany). All immunofluorescence images were taken by inverted fluorescence microscope (Axio Observer Z1, ZEISS, Oberkochen, Germany).

3.3 Fabrication of Optoelectronic Biointerfaces and integration of MnO2 Nanoflowers

The fabrication process of MnO2 nanoflowers for integration into the flexible optoelectronic biointerface involved several specific steps, including preparing the seed layer and the subsequent growth of the nanoflowers using chemical bath deposition. Here, we provide a detailed description of the fabrication process, including deposition parameters and any challenges encountered. However, the detailed preparation, concentration, and parameters are given in chapter '3.2' for those who need more details.

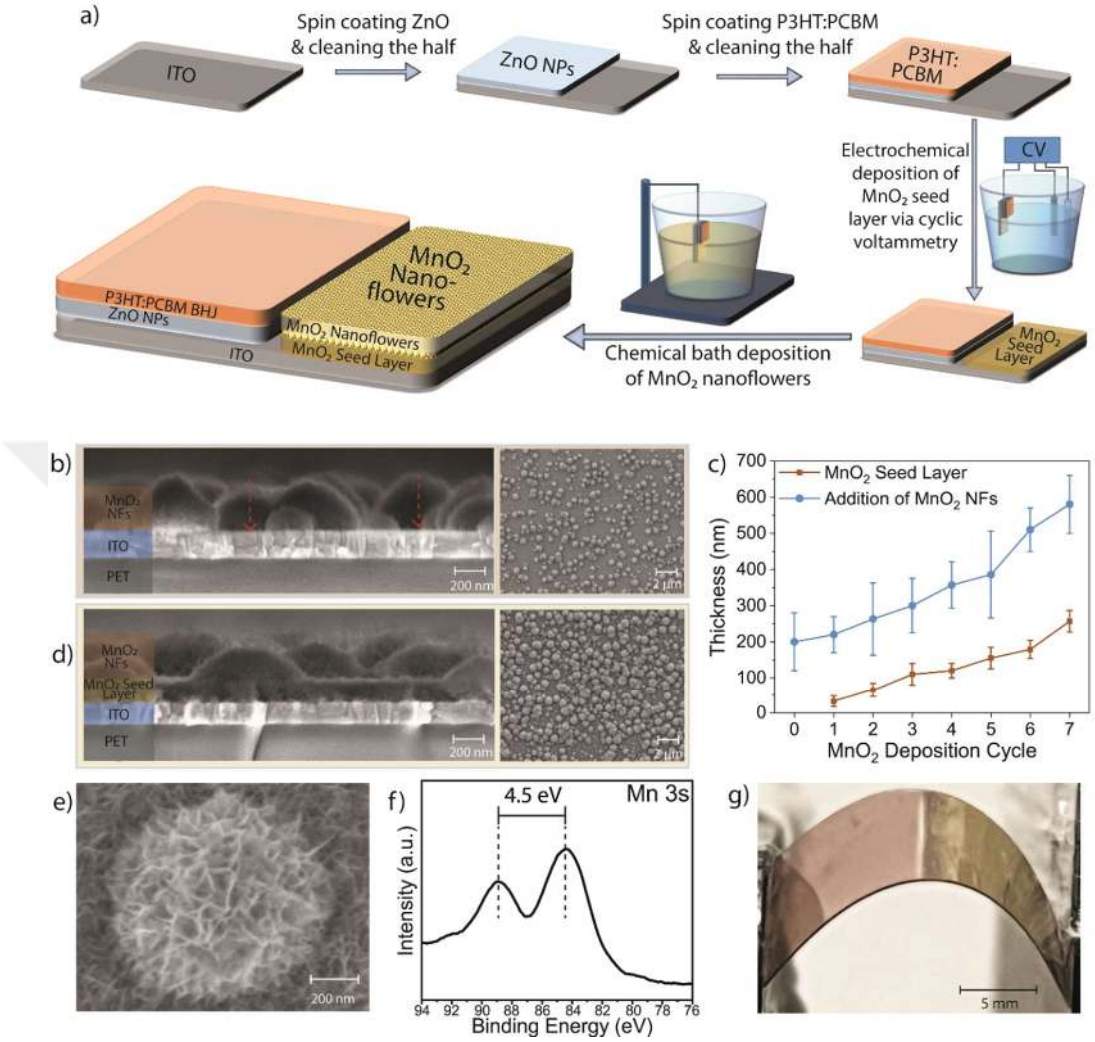

Figure 3.1 a) The fabrication flow schematic of MnO_2 nanoflower integrated optoelectronic biointerface. (Not drawn in scale). b) (Left) Cross-sectional FESEM (field emission scanning electron microscopy) of the return electrode without MnO_2 seed layer. The red arrows show the regions that create unwanted electrical pathways between the ITO layer and the electrolyte. (Right) Top FESEM view of the structure. c) The thickness of the MnO_2 seed layer and nanoflower-modified seed layer as a function of the seed layer deposition cycle. d) (Left) Cross-sectional FESEM of the return electrode after the nanoflower growth on the seed layer. (Right) Top FESEM view of the structure. e) Top FESEM view of a MnO_2 nanoflower. f) High-resolution XPS spectrum of Mn 3s. g) Photograph of the flexible optoelectronic biointerface. The left half (pinkish) is the photoactive part, and the right half (yellowish) is the return electrode with nanoflowers.

Glass or PET substrates covered with indium tin oxide (ITO) were used as the base for fabricating the photoelectrodes. The substrates were cleaned and disinfected carefully. The optoelectronic biointerfaces are fabricated by sequential spin coating and cleaning cycles for the photoactive part, which is followed by nanoflower synthesis on the return

electrode (Figure 3.1a). First, ZnO nanoparticles (NPs) are spin-coated on indium tin oxide (ITO), and annealing is done to form a uniform NP layer. Then, poly(3-hexylthiophene-2,5-diyl):[6,6]-phenyl-C61-butyric acid methyl ester (P3HT:PCBM) bulk heterojunction (BHJ) thin film is spin-coated with an optimized concentration (Figure 3.2). For optimization, we varied the concentration of the coating solution of the photoactive layer while keeping the spin speed fixed at 1500 rpm (Figure 3.2). The increase in concentration directly affects the conversion of light to ionic currents, and after the concentration of 60 mg $ml^{-1,}$ the photocurrent starts to drop, possibly due to the limited electron and hole diffusion in thicker layers.

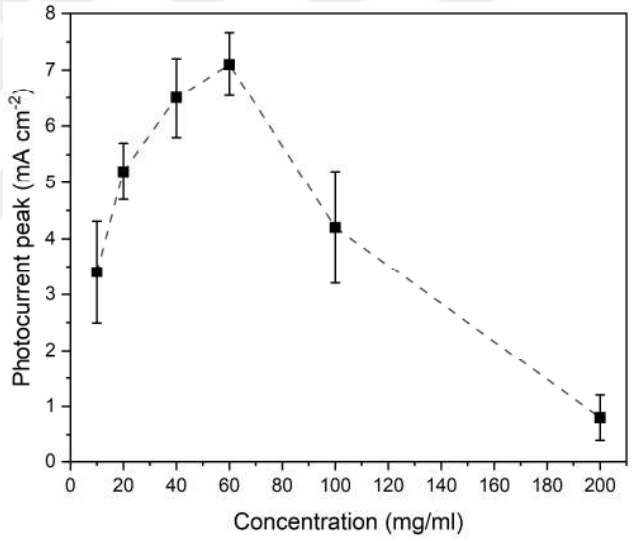

Figure 3.2 Optimization of peak photocurrent density by varying the spin-coated P3HT:PCBM concentration.

After each step, half of the device is cleaned to keep the return electrode area uncoated. Thus, the photoactive part of the neural interface is formed on one half of the device, while unmodified ITO is on the other half. Afterward, MnO_2 nanoflowers are directly formed via chemical bath deposition on top of the ITO (Figure 3.1b). However, the direct formation of MnO_2 NFs leads to incomplete coverage of the ITO layer, which forms unwanted shunt impedance at the electrode-electrolyte interface and decreases the interfacial capacitance (Figure 3.3).

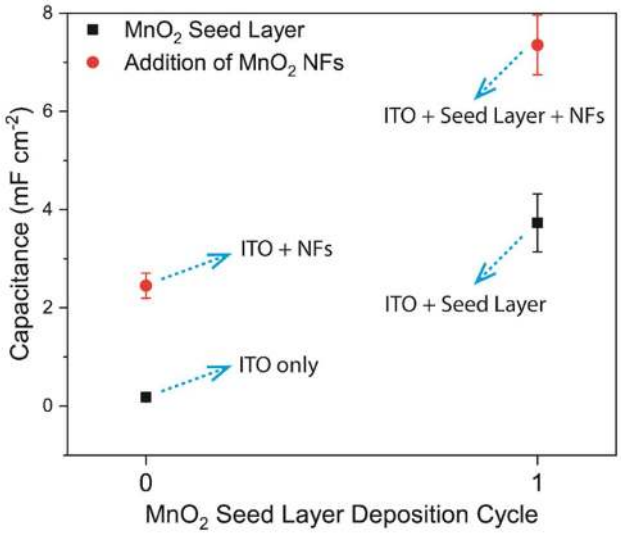

Figure 3.3 The effect of layers on the capacitance of various return electrodes.

As a solution, the MnO_2 seed layer is initially formed on ITO via cyclic voltammetry (CV) deposition, and afterward, the nanoflowers are grown via chemical bath deposition. The seed layer is deposited by submerging the return electrode region (i.e., ITO) into $MnSO_4$: Na_2SO_4 aqueous solution [57]. The thickness of the seed layer can be adjusted by increasing the CV cycle (Figure 3.1c). After each cycle, an average thickness of 33 nm (± 12 nm) is deposited, and ITO is homogeneously covered after five cycles of seed layer deposition with a mean thickness of 110 nm (± 30 nm). Then, to form nanoflowers on the seed layer, a MnO_2 nanoflower layer is formed on top of the seed layer by chemical bath deposition via immersing the return electrode into the highly concentrated Na_2SO_4: $MnSO_4$:$K_2S_2O_8$ aqueous solution [58]. Once this step is completed, MnO_2 nanoflowers (with a mean size distribution of 279 nm ± 169 nm) (Figure 3.4a) are formed onto the MnO_2 seed layer. Using our deposition technique, we observed nanoflowers of different sizes, and the average size was 279 nm with a standard deviation of 169 nm (Figure 3.4a).

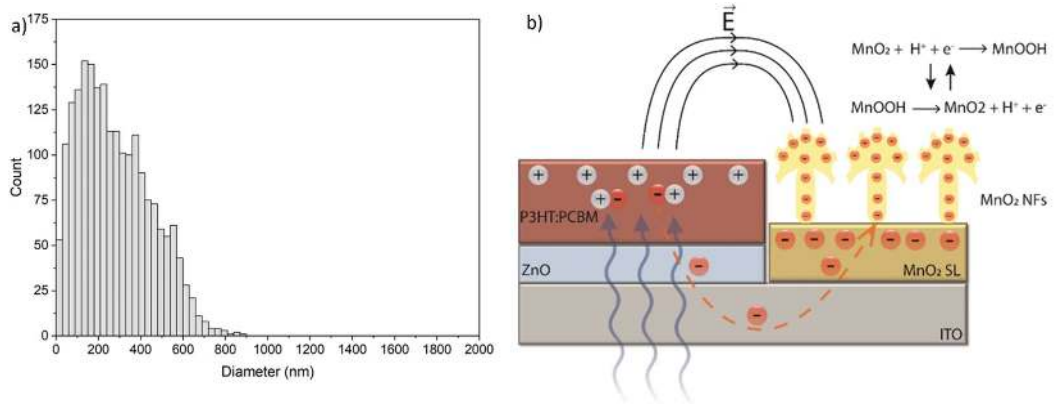

Figure 3.4 a) MnO_2 nanoflowers size distribution histograms obtained from SEM images (n>2000). According to the Gaussian distribution, the mean is 279 nm, and the standard deviation is 169 nm. b) Cross-sectional schematic of charge movement under light illumination with charge storage reactions.

The MnO_2 seed layer facilitates enhanced nanoflower density during chemical bath deposition while the chemical bath deposition parameters, as in the case of nanoflower growth on ITO, were kept constant (Figure 3.1d). Advantageously, the FESEM image of a single MnO_2 NF on the seed layer illustrates the nanomorphology with a high surface area (Figure 3.1e). Moreover, the MnO_2 seed layer facilitated a complete MnO_2 and electrolyte interface without ITO.

The cross-sectional schematic of the device is given in Figure 3.4b to understand charge movement and injection mechanism better. When the incoming light (blue rays) enters the system (Figure 3.4b), they cause impairment of electrons and holes. The holes are trapped in the photoactive P3HT:PCBM layer due to the hole-blocking properties of ZnO, while the electrons travel through the ZnO and ITO layers to reach the MnO_2 return structure at lower energy levels. This rapid movement produces a capacitive spike in the current due to the presence of an electrical double layer. Subsequently, the electrons on the surface of the MnO_2 nanoflowers initiate the reduction reaction depicted in Figure 3.4b, leading to faradaic charge injection and slower current decay during illumination (Figure 3.6c). When the light source is turned off, the available electrons return to the photoactive layer and recombine, resulting in the rapid, reverse capacitive spike observed in Figure 3.6c at 30 ms. The oxidation reaction occurs, which causes the charge injection and slow current decay after 30 ms (Figure 3.6c). This structure offers several advantages

for neural stimulation. The high surface area of the MnO_2 nanoflowers reduces impedance (Figure 3.6e). It allows for more surface faradaic reactions, while the short distance between positive and negative charges creates strong electrical fields crucial for stimulating neurons. And this local return structure is essential for building pixelated devices in the future for high-resolution stimulation [18].

X-ray photoelectron spectroscopy (XPS) was performed to study the composition of the manganese oxide nanoflowers (Figure 3.5). According to the XPS survey spectrum (Figure 3.5a), there are 3 main elements: Mn, O, and C. The peaks at 495-486 eV and 451.9-444.8 eV are attributed to the ITO substrate, which has Sn 3d and In 3d peaks. Figure 3.5b demonstrates the Mn 2p spectra of the manganese oxide flowers. Two signals are detected at around 641.9 and 653.6 eV due to the spin-orbit coupling [62], which can be ascribed to the binding energies of Mn $2p_{3/2}$ and Mn $2p_{1/2}$, respectively [63, 64]. The energy difference between these signals is 11.7 eV, consistent with the previously reported data for Mn $2p_{3/2}$ and Mn $2p_{1/2}$ in MnO_2 [65]. Moreover, we performed an XPS analysis on the Mn 3s region. This analysis observed two distinct peaks at energy levels of 84.4 eV and 88.9 eV. The multiplet splitting, measured at 4.5 eV (Figure 3.5c), suggests the predominant presence of Mn (IV) oxidation states, in agreement with the previous literature [66] that indicates the existence of MnO_2. The high-resolution O 1s spectrum deconvoluted into two peaks, 529.6 and 531.1 eV, using the XPS best peak fitting with Gaussian modes (Figure 3.5d). According to the literature, these peaks can be attributed to Mn–O–Mn and Mn–O–H bonding, respectively [59]. Also, the high-resolution C 1s spectrum of MnO_2 is shown in Figure 3.5e C-C, C-O, and C=C peaks are deconvoluted at 284.5, 286.1, and 287.9 eV with the best fitting of Gaussian modes. During this analysis, all the peaks were adjusted based on the C 1s standard peak of 284.5 eV.

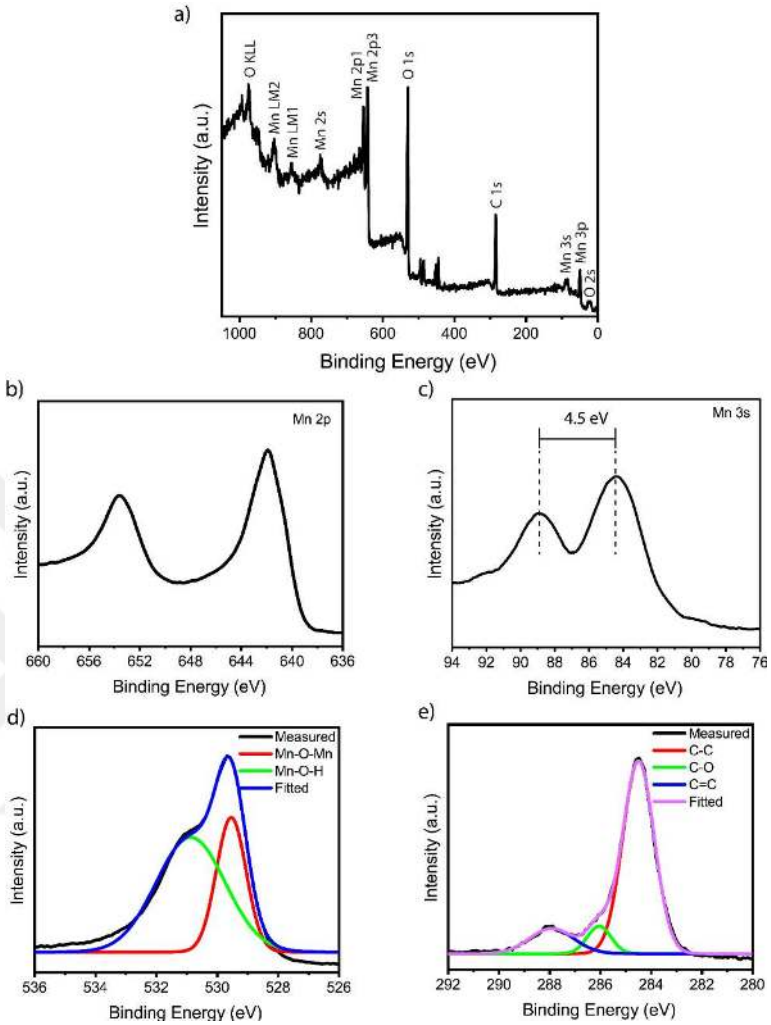

Figure 3.5 XPS spectra for MnO_2 nanoflowers a) survey spectrum and high-resolution spectra for b) Mn 2p, c) Mn 3s, d) O 1s, and e) C 1s.

To better understand the oxidation states of the manganese, we also conducted the XPS analysis in the Mn 3s region (Figure 3.1f). The Mn 3s spectrum exhibited two peaks located at 84.4 eV and 88.9 eV. The multiplet splitting of the Mn 3s peaks was 4.5 eV, which corresponds to mainly Mn (IV) oxidation states indicating MnO_2 [66]. The whole solution-processed fabrication procedure can be directly used to fabricate devices on flexible substrates (e.g., PET) (Figure 3.1g), which is beneficial for having conformal contact with tissues [23, 24].

3.4 Electrochemical Characterization

To quantify the contribution of MnO_2 NFs on the overall device performance, we measured the short circuit photoresponse via a potentiostat/galvanostat instrument. For that, we utilize an electrochemical setup with three electrodes. The working electrode is connected to the ITO, the Ag/AgCl is the reference electrode, and the platinum is the counter electrode (Figure 3.6a). The photovoltage of the optoelectronic biointerface and the control group (without MnO_2) are quantified under 20 ms light pulses with various light intensity levels (Figure 3.6b). In our electrochemical system, we used the biological fluid of artificial cerebrospinal fluid (aCSF) solution to understand the operating performance in physiological conditions. We observed the photovoltages of 260 mV under light illumination with the intensity of 99 mW cm^{-2}, comparable to the previously reported retina implants [56].

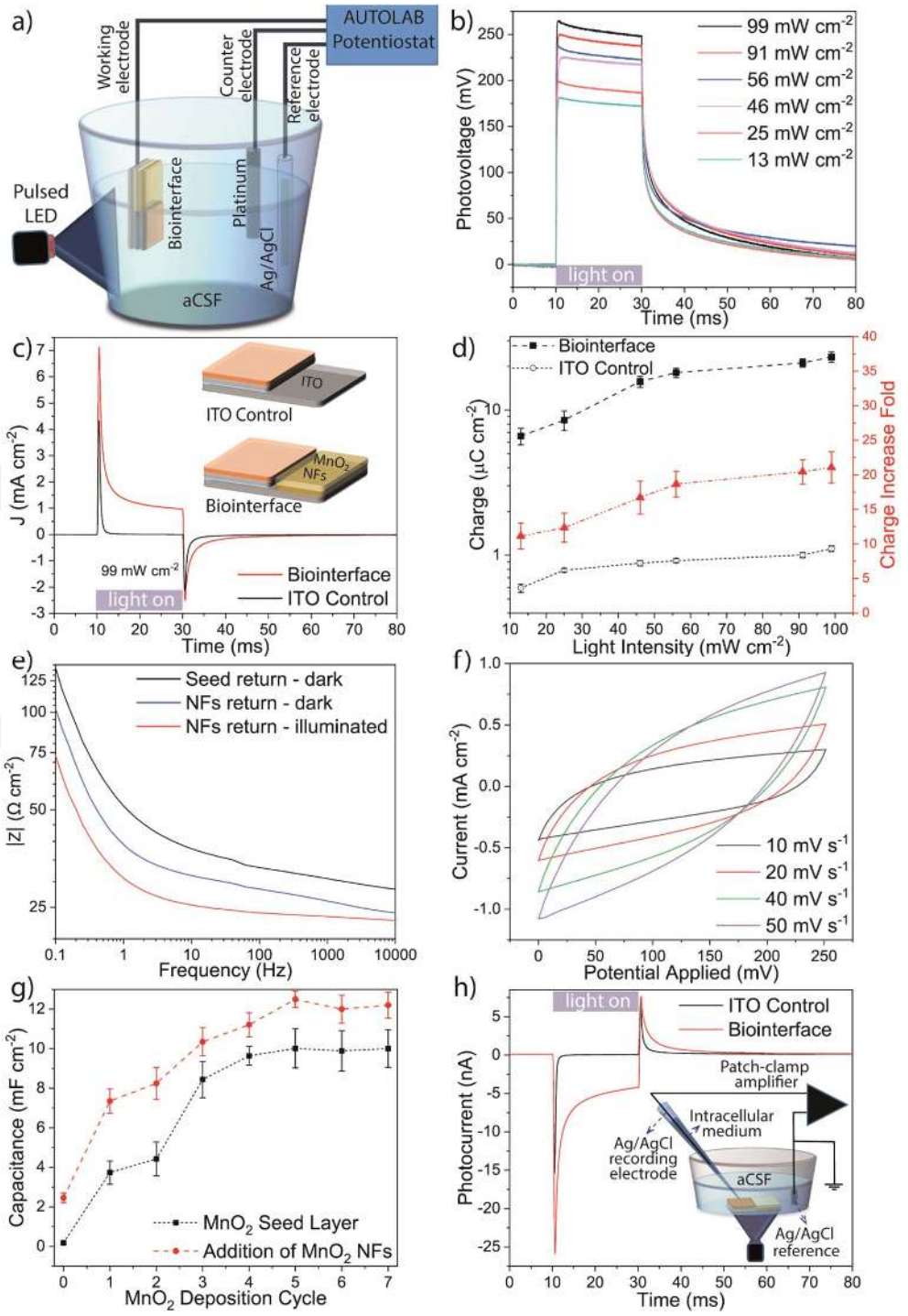

Figure 3.6 a) The schematic of the three-electrode AUTOLAB potentiostat for photocurrent and photovoltage characterization of the optoelectronic biointerfaces. b) Photovoltage of the biointerface under different light intensity levels (λ= 450 nm). c) Photocurrent density of the biointerface and ITO control (i.e., biointerface with ITO return electrode) under the illumination of 99 mW cm^{-2}. Inset shows the schematic of the measured devices. d) Charge injection density of the biointerface and ITO control in aCSF (left axis) and fold of charge increase of the biointerface compared to ITO control (right

axis) under different light intensities (mean ± SD for n = 10). e) Bode modulus of the seed layer and return electrode with nanoflowers under dark and light (99 mW cm^{-2}) in the frequency range of 0.1Hz - 10 kHz. f) Cyclic voltammograms of the return electrode in the range of 0-250 mV as a function of scan rate. g) The capacitances of the return electrodes on the seed layer with and without nanoflowers. h) The measured photocurrents of the biointerface and ITO control over the surface of the photoactive regions under the illumination of 99 mW cm^{-2}. Patch-clamp pipettes in the electrophysiology setup were used without any wire connection. Inset shows the simplified schematic of the measurement configuration.

Figure 3.6c shows the current density per area of the biointerface. Compared with the control group, the MnO_2 NF integration facilitates a 21-fold increase of the ionic charge levels, which significantly improves the effective photostimulation of neurons. Though the photocurrent peak was increased only 1.5-fold, the increment in the charge was drastically enhanced by more than 20 folds because of the slower decay of the photocurrent. We calculated the device's responsivity (peak photocurrent/illuminated light power) and the external quantum efficiency (number of generated ionic charges/externally applied number of photons). The responsivity corresponds to 70.53 mA $W^{-1,}$ and the external quantum efficiency for a 20 ms light pulse is 0.034 ion per photon. We investigated the injected charge density for the biointerface and the control under various light intensities (Figure 3.6d), and the biointerface generates significantly higher charge densities than the control. The charge density levels are sufficient to stimulate different human tissue in vivo, such as the human subthalamic nucleus, sub-retina, and cortical part of the brain [67, 68]. Figure 3.6e shows that the impedance is decreased after adding NFs under dark. Compared with the seed layer, the impedance decrease originates from the branched walls of nanoflowers with a larger effective surface area because of the nanosized petals and conduits. Moreover, the impedance further decreases under illumination.

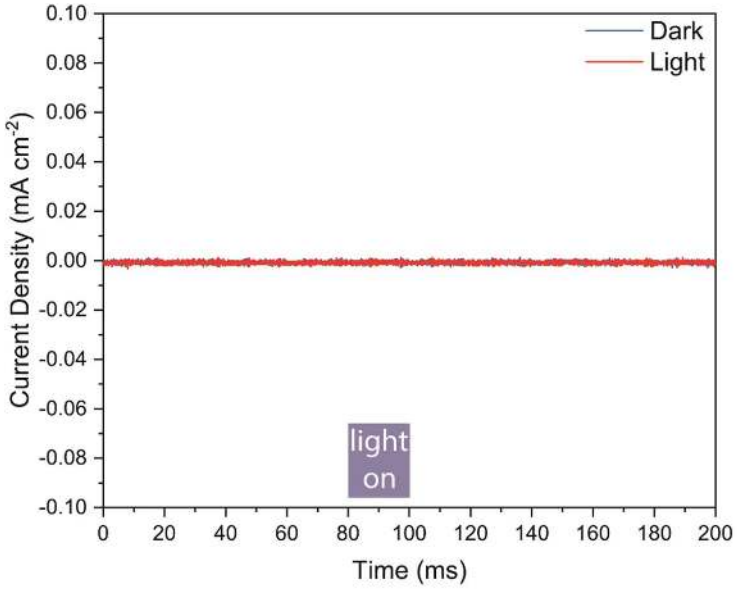

Figure 3.7 The current density of only MnO_2 return structure under the dark and light. The blue square represents the light pulse.

To evaluate the charge generation and storage behavior, the cyclic voltammograms (CV) of NFs within the device operation potentials were recorded, and they reveal capacitive-like current-voltage behavior (Figure 3.6f). The quasi-rectangular shapes of the CV show the presence of reversible redox reactions and the pseudocapacitive behavior of the interface, which is critical for the safe photostimulation of neurons and for keeping the cellular environment healthy for cells. Here the reversibility of the Faradaic reactions originates from the surface adsorption and intercalation/deintercalation of electrolyte cations of Na^+ and K^+ that are involved in the aCSF solution [69]. Moreover, since the operation range of our device is within the working potential window (WPW) of MnO_2 (-0.2 to 1.2 V), this suppresses irreversible hydrogen and oxygen redox reactions [41]. We checked the photoactivity of the MnO_2 NFs and observed that it could not induce any photocurrent (Figure 3.7). Thus, the increase in the photocurrent and charge injection density is solely due to the pseudocapacitive behavior of the nanostructured return electrode.

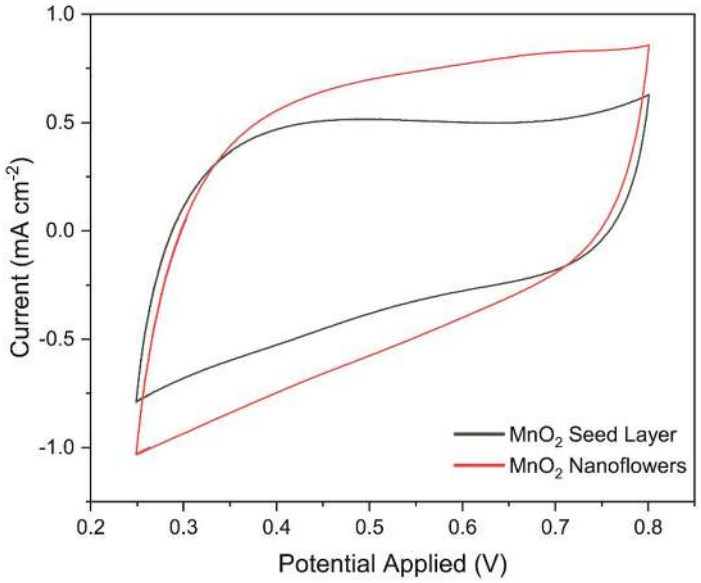

Figure 3.8 Cyclic voltammograms of MnO_2 seed layer and MnO_2 NFs on the seed layer (scan rate: 50 mV s^{-1}).

To quantify the capacitance levels, we integrated the area under the CV curves (Figure 3.8). The seed layer directly affects the capacitance, which increases with the number of deposition cycles and saturates due to the limited diffusion of the electrons after five cycles. On top of the seed layer, the growth of MnO_2 NFs increases the capacitance of the return electrode structure because of the enhanced surface area (Figure 3.6g & Figure 3.8). During its operation in a cellular environment, the biointerface stimulates neurons without any wire connection; hence the waveshapes and the increase of the charge injection levels are also confirmed by electrophysiology measurement setup under such a wireless condition, which consists of a recording electrode inside a thin glass pipette filled with intracellular solution and a distant reference bath electrode in the aCSF with a patch clamp amplifier (Figure 3.6h inset) [70]. Likewise, the photocurrent peak was also increased 1.5-fold, and a similar waveshape of the device was observed (Figure 3.6h).

3.5 Stability and Biocompatibility

We investigate the stability and biocompatibility of the MnO_2 nanoflower integrated optoelectronic biointerface. The photocyclic stability study reveals that the biointerface has a charge injection performance of 76 ± 7% after 20000 illumination cycles (Figure 3.9a). The electrochemical stability of MnO_2 NFs is evaluated by repetitive CV characterization, and the area enclosed by CV graphs, which is correlated with capacitance, remains the same for the 10000 cycles showing the excellent stability of nanoflowers (Figure 3.9b). One of the critical steps of cellular experiments is the sterilization of the biointerface. We confirm that the biointerface retains 92 ± 6% of its charge injection after the stabilization steps of ethanol and UV treatment (Figure 3.9c).

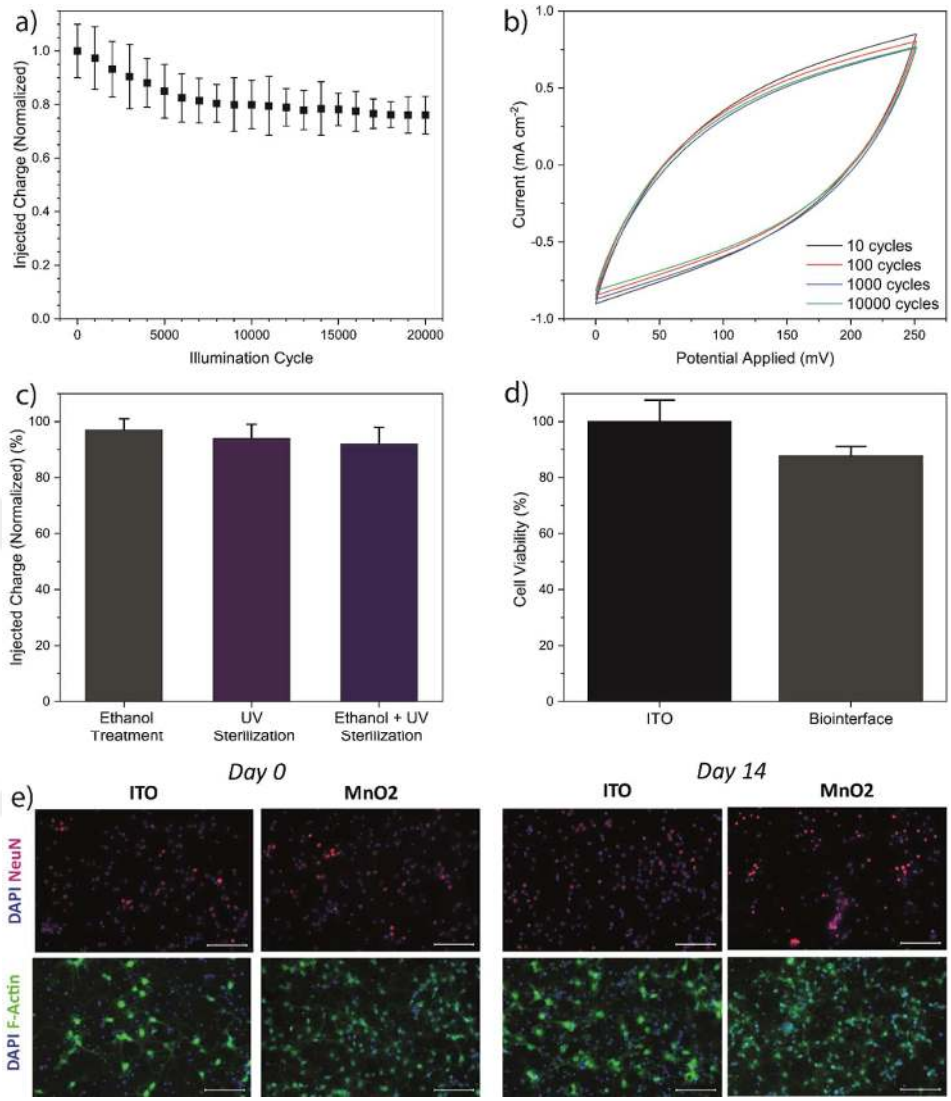

Figure 3.9 a) Charge injection stability of MnO_2 optoelectronic biointerface for 20000 photo-cycles (mean ± SD for n = 5). Illumination parameters are 450 nm wavelength, 20 ms pulse width, 1 Hz illumination frequency, and 99 mW cm^{-2} light intensity. b) Cyclic voltammogram stability of nanoflowers up to 10000 cycles. Measurement parameters are 40 $mV.s^{-1}$ scan rate and 0 - 250 mV potential window. c) Change in normalized charge injection after sterilization steps of the optoelectronic biointerface (mean ± SD for n = 4). d) CTG cytotoxicity assay for quantifying cell viability of primary hippocampal neurons cultured on the biointerface and control ITO devices (mean ± SEM for n = 4). An unpaired, two-tailed t-test was used for statistical analysis, and $*p < 0.05$ was evaluated as statistically significant. e) Immunofluorescence images of cells cultured on the biointerface and control ITO devices on days 0 and 14 to observe the morphology and viability of primary hippocampal neurons. Cells were co-stained with DAPI (blue) to show the nucleus, Anti-NeuN (red) to show the neuronal nucleus, and Anti-f-Actin (green) to indicate cell structure (scale bar: 100 µm).

After stability characterizations, we conduct biocompatibility experiments. The cell viability experiments are performed with primary hippocampal neurons cultured on the biointerface and ITO control substrates. After 3 days of neuron culture on substrates, a CTG assay is performed to examine the cytotoxicity, and the biointerface has comparable viability with the ITO substrates (Figure 3.9d). Moreover, day 0 and day 14 cultures show short- and long-term morphological changes and neural network improvements on the biointerface and ITO control substrates. We confirm neuron survival and maintenance of their characteristics on the biointerface after 2 weeks of culture by immunofluorescence staining of anti-NeuN, a neuronal nuclear protein, and f-Actin, cytoskeleton filaments (Figure 3.9e).

3.6 Electrophysiological Characterization

To test the light-induced stimulation of neurons, we execute single-cell patch clamp recordings with primary hippocampal neurons cultured on the biointerface [71, 72]. We use an Ag/AgCl electrode in the pipette filled with the intracellular solution as the recording electrode and a distant Ag/AgCl reference electrode (Figure 3.10a). We record the electrical activity of neurons in the whole-cell configuration (Fig. 4a inset), and the biointerface operates in open-circuit conditions without any wire connection. First, we check the required membrane depolarization for the stimulation of neurons. The cell membrane potential is held at different holding potentials, and the transmembrane current is recorded in voltage-clamp mode under dark conditions. The values higher than -40 mV cause the opening of the voltage-gated sodium channels, which indicates the possibility of the firing of an action potential (Figure 3.10b). For -20 mV and -30 mV holding potentials, the fast sodium inward currents are followed by slower potassium outward currents. Moreover, the sodium gate activation delay is less for higher potentials due to a larger amount of depolarization in the same time interval.

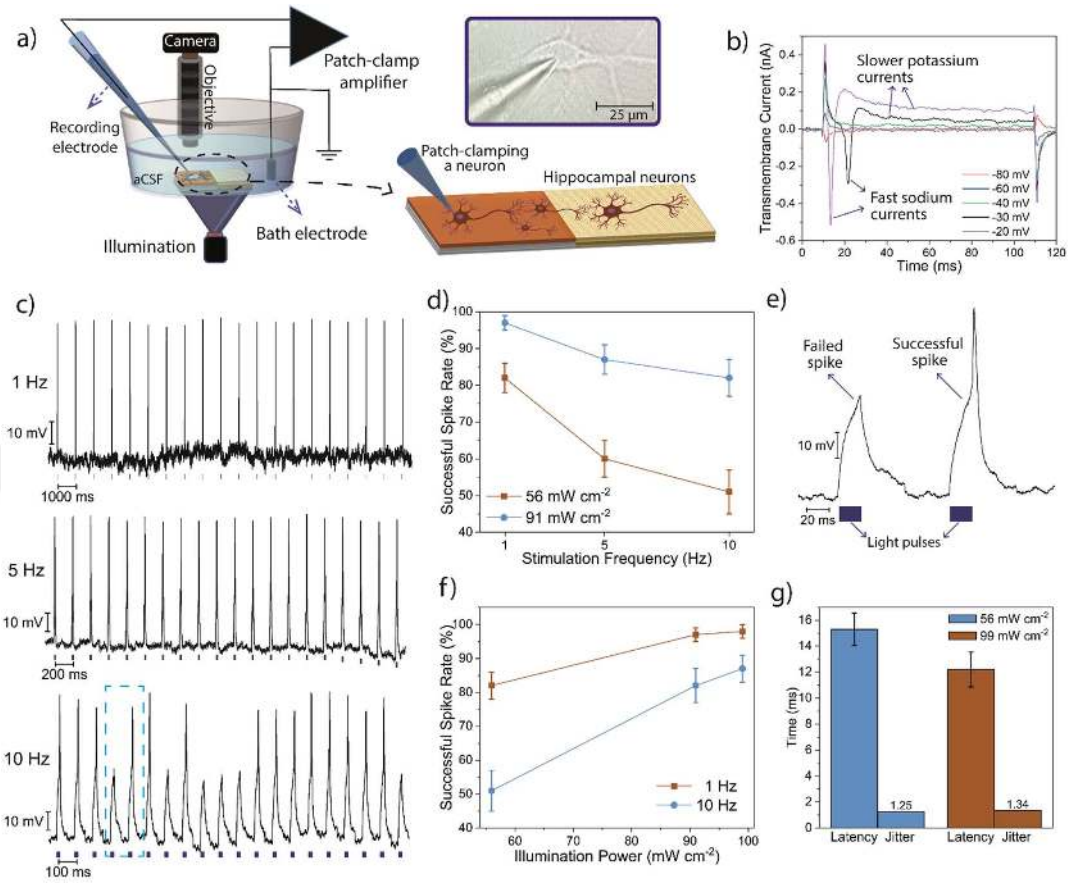

Figure 3.10 a) The schematic of the patch-clamp electrophysiology recording setup. Inset (Down): The schematic of patching of a neuron. Inset (Top): Photograph of a patched neuron. b) Transmembrane current of a patched neuron under whole-cell recording for different holding potential levels. c) Current-clamp recording of primary hippocampal neurons under photostimulation of different frequencies for 1, 5, and 10 Hz. The wavelength of light is 445 nm, the illumination intensity is 91 mW cm^{-2}, and the duration of each pulse is 20 ms (the small rectangles represent light pulses). The area enclosed by dashed blue lines is zoomed in Figure 3.10e. d) Stimulation frequency dependence of successful spike rate for 56 and 91 mW cm^{-2} with a duration of 20 ms (mean ± SD for n = 6). e) Failed and successful action potential traces at 10 Hz. f) Illumination power dependence of successful spike rate for 1 and 10 Hz (mean ± SD for n = 6). g) Latency and jitter of the biointerface under the illumination of 56 and 91 mW cm^{-2} (pulse duration of 20 ms; frequency of 1 Hz) (mean ± SD for n = 6).

For the photostimulation of neurons, we apply light-pulse trains at different frequency levels (1-10 Hz) while recording the membrane potential under current-clamp mode. At 1 Hz, we can observe highly repetitive and successful action potential generation (Figure 3.10c (top)). After an initial capacitive spike induced by the light onset, the biointerface continuously injects charges during 'light-on' periods owing to the

MnO_2-induced reversible electrochemical reactions at the device-electrolyte interface, which is followed by the second capacitive spike at the light offset (Figure 3.11).

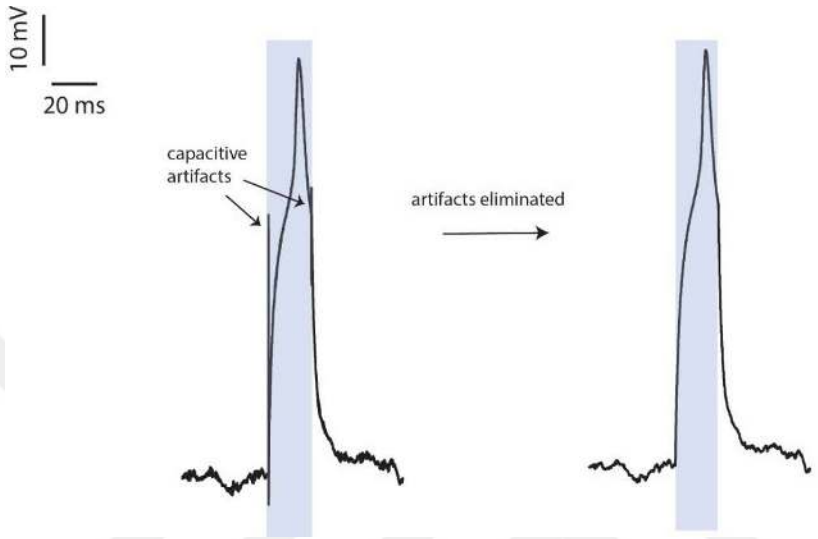

Figure 3.11 Current clamp recording trace showing the capacitive stimulation artifacts at the light onset and offset. Blue bars show the 20 ms 'light on' period. The artifacts are eliminated via downsampling and smoothing, which remains the characteristics of the action potential, such as threshold voltage, peak magnitude, and latency intact.

The charge injection during 'light-on' periods leads to hyperpolarization of the attached membrane and depolarization of the free membrane, which leads to the firing of neurons above the threshold [73]. The success rate decreases for identical illumination power as we increase the frequency (Figure 3.10d & 4e). To compensate for the decrease in the successful spike rate, we applied higher light intensities, which led to higher success for the photostimulation of neurons (Figure 3.10d, 4f). AP latency (time between the start of the illumination and AP peak) and jitter parameters are shown in Figure 3.10g for different illumination powers. The lower latency for greater light intensity is due to the higher charge density levels in the identical time interval. The latencies are significantly lower than other recent optical stimulation techniques, such as photothermal and photoacoustic stimulation [74, 75], and similar to the range observed in optogenetics [76, 77]. Since certain neural activities have millisecond or sub-millisecond spike timing precisions [78, 79], such latency and jitter levels are advantageous for inducing

temporally precise action potentials and minimizing the temporal variabilities across neurons to examine neural mechanisms with higher accuracy [80, 81].

3.7 Discussion

This study demonstrated the successful integration of nanoflowers into flexible optoelectronic biointerfaces for effective photostimulation of neurons. In addition to nanoflowers, other nanomorphologies such as nanocubes, nanowires, nanorods, and hollow spheres can also be deposited using a similar electrochemical approach[69]. Furthermore, MnO_2 can be chemically modified by mixing it with other transition metal elements and doping it with metallic elements such as Al, Sn, and Pb, providing tunability of electrical properties for cell interfaces [82-84]. Tuning nanomorphology and electrical properties holds high potential for developing pixilated device structures with microscale stimulation electrodes. The impedance increases as the electrode size decreases and the charge injection capacity decreases. To overcome this issue, the use of materials with high reduction-oxygen capacity and electrochemical surface area is necessary[85]. Therefore, integrating pseudocapacitive materials with enhanced surface area via 3D nanostructures has a high potential for developing miniaturized and flexible bioelectronic devices.

Table 3.1 Photocurrent, charge density, excitation wavelength, light intensity and optical pulse duration in previous reports.

References	Photocurrent	Charge density	Wavelength	Light intensity or Light power	Optical pulse duration
This study	7.1 mA cm^{-2}	23.2 μC cm^{-2}	450 nm	0.99 mW mm^{-2}	20 ms
[43]	6 mA cm^{-2}	20 μC cm^{-2}	450 nm	0.87 mW mm^{-2}	10 ms
[29]	0.5 mA cm^{-2}	6 μC cm^{-2}	780 nm	1 mW mm^{-2}	20 ms
[23]	2 mA cm^{-2}	7.5 μC cm^{-2}	638 nm	8.5 mW mm^{-2}	5 ms
[10]	3 mA cm^{-2}	1 μC cm^{-2}	445 nm	1.5 mW mm^{-2}	50 ms
[86]	125 μA cm^{-2}	1.29 μC cm^{-2}	445 nm	0.57 mW mm^{-2}	10 ms
[87]	0.6 mA cm^{-2}	0.18 μC cm^{-2}	445 nm	1 mW mm^{-2}	20 ms

[88]	55 μA cm^{-2}	0.45 μC cm^{-2}	445 nm	0.57 mW mm^{-2}	10 ms
[89]	800 μA cm^{-2}	8 μC cm^{-2}	630 nm	0.33 mW mm^{-2}	10 ms
[90]	13 nA	8 pC	Warm white	180 mW	100 ms
[91]	4.5 nA	6.97 pC	445 nm	0.42 mW mm^{-2}	10 ms
[54]	135 μA cm^{-2}	-	565 nm	0.94 mW mm^{-2}	200 ms
[92]	200 pA	-	532 nm	15 mW mm^{-2}	20 ms
[50]	60 nA	-	530 nm	6 mW mm^{-2}	10 ms
[8]	400 μA	-	660 nm	0.6 mW mm^{-2}	5 ms
[93]	300 pA	-	450 nm	1.69 mW mm^{-2}	500 ms

MnO_2 nanoflowers beneficially show a lower impedance than our previous studies using RuO_2 [43]. MnO_2 nanoflowers also decrease the impedance in comparison with its seed layer as well (Figure 3.12). Compared with previous state-of-the-art organic optoelectronic biointerfaces, the optimized device can facilitate a higher photocurrent and charge level (Table 3.1). In addition, photoresponse under near-infrared (NIR) light illumination within the tissue transmission window can be obtained by replacing the photoactive layer with NIR-responsive organic or inorganic materials such as PCPDTBT:PC60BM [94] or PbS quantum dots [29], respectively.

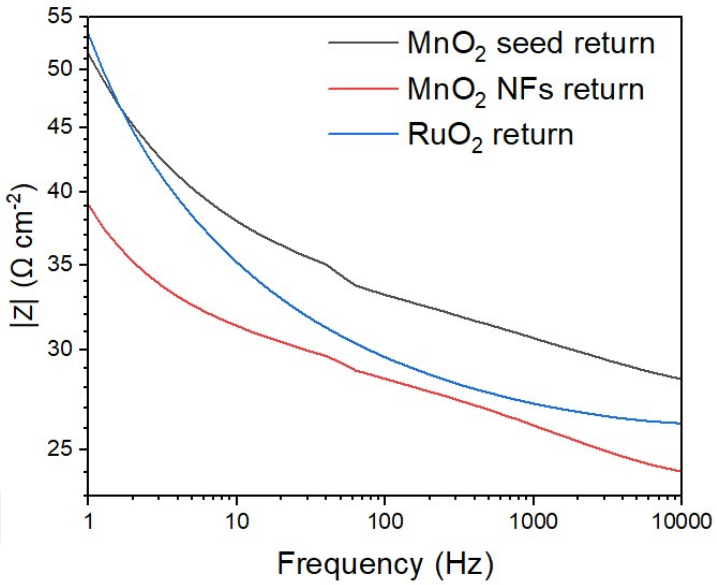

Figure 3.12 Impedance of MnO_2 seed, MnO_2 NFs and RuO_2 return in the frequency range of 1Hz - 10 kHz

Alternative to ITO, MnO_2 nanoflowers can also be formed on FTO, gold, and stainless steel (Table 3.2). To demonstrate this, we experimented on FTO substrates and obtained comparable photocurrent, photovoltage values, and similar capacitance values for the MnO_2 return electrode. For MnO_2 coating on FTO, we used 12 mV s^{-1} and 6 deposition cycles, followed by the chemical bath deposition. Additionally, we deposited the MnO_2 seed layer on gold and stainless steel substrates with slightly altering electrochemical deposition parameters. Since the thin gold layer is more conductive, we decrease the step voltage to 4 mV s^{-1} and the deposition cycle to 2 with the same deposition duration. Similarly, we used 2 mV s-1 step voltage for stainless steel mesh and 1 deposition cycle. The chemical bath deposition duration remained the same for all the substrates, with a slight alteration in bath temperature and annealing temperature (Table 3.2). The formation of MnO_2 nanoflower is also visualized by SEM (Figure 3.13). Besides these substrates, MnO2 flowers can also be obtained on graphene, graphite, and zeolitic imidazolate framework [59-61].

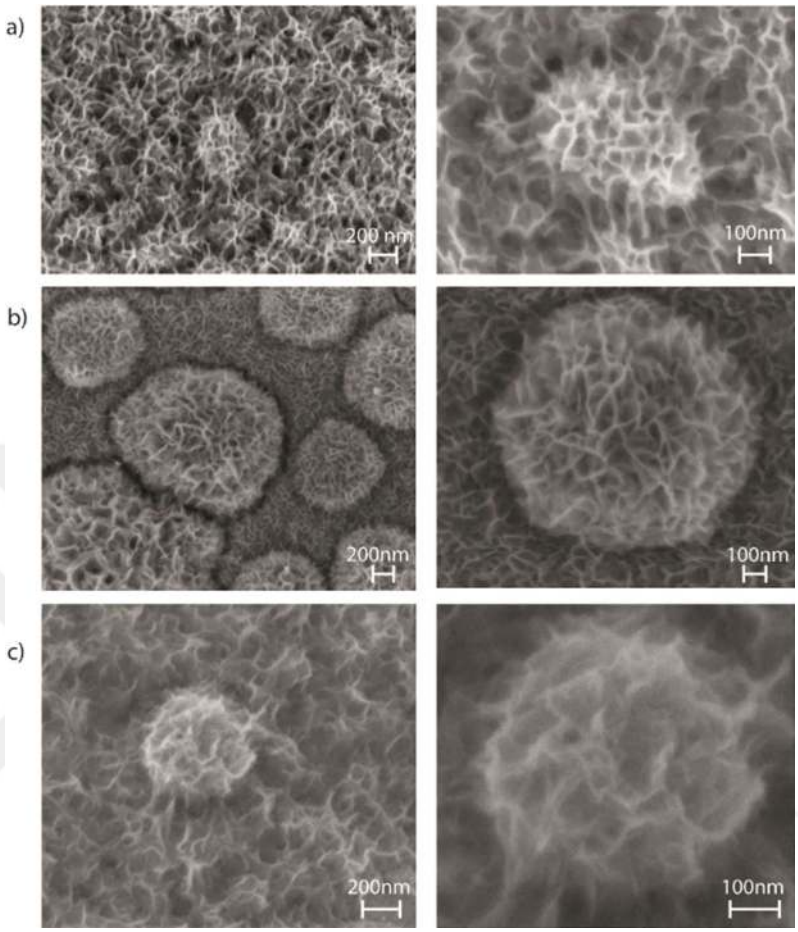

Figure 3.13 The SEM images of MnO_2 NFs coated on a) FTO, b) gold, and c) stainless steel substrates.

Other materials can be used in nanoflower form, such as nickel hydroxide ($Ni(OH)_2$) [32], cobalt oxide (Co_3O_4)[31], copper oxide (CuO)[34], zinc oxide (ZnO)[33], and ruthenium oxide (RuO_2) [35]. Even though $Ni(OH)_2$ and Co_3O_4 have higher capacitance, however, they are not suitable for in vivo application as $Ni(OH)_2$ is highly toxic, and Co_3O_4 can release significant amounts of ROS (reactive oxygen species) during in vivo applications [95]. The remaining metal oxides are the best contenders as supercapacitor electrode materials for bioelectronics owing to their wide variety of oxidation states, which are suitable for safe charge transfer. Compared to CuO and ZnO, MnO_2 and RuO_2 have higher capacitance, but the high impedance of metal oxides generally presents a drawback [96]. To decrease the impedance, a nanoflower morphology can be added (Figure 3.6e). Since the formation of RuO_2 nanoflowers are comparatively much longer

and more complex [35], we selected MnO_2 material for nanoflowers that can be deposited to the return electrode in a few hours with a simple fabrication procedure. In addition, MnO_2 is an ideal electrode material due to its non-toxic nature, abundancy, low cost, wide potential range, high electrochemical activity, high theoretical capacity (1370 F g^{-1}), adjustable thickness and shape via coating method and parameters. Its biocompatibility is another advantage for the biointerface application. Therefore, we selected MnO_2 for neural stimulation.

Table 3.2 Deposition parameters of MnO_2 nanoflowers on different substrates.

		Electrochemical Deposition Parameters			Chemical Bath Deposition Parameters		
		Step Voltage (mV s^{-1})	Deposition Cycle	Annealing temperature (°C)	Bath Temperature (°C)	Bath Duration (Hour)	Annealing temperature (°C)
Substrate	**ITO**	**10**	**5**	**50**	**60**	**2**	**70**
	FTO	**12**	**6**	**80**	**70**	**2**	**90**
	Gold	**4**	**2**	**50**	**60**	**2**	**70**
	Stainless steel	**2**	**1**	**70**	**80**	**2**	**90**

MnO_2 is a well-known material for energy storage devices [36], and its nanostructures have recently attracted significant attention for biomedical applications. For instance, MnO_2-based nanoscaffolds have been found to enhance the adhesion of stem cells, promote their differentiation into neurons, and facilitate neurite outgrowth for stem cell transplantation [97]. Furthermore, MnO_2 nanoparticles possess immunomodulatory properties for cancer starvation therapy and can induce oxidative stress and autophagy in nutrient-deprived cancer cells [98]. Additionally, MnO_2 nanosheets have been utilized for biocatalysis, fluorescence quenching in biosensing, and MRI-contrast agents [99]. Therefore, this first study, employing MnO_2 nanostructures for the photostimulation of neurons, can be combined with different forms of MnO_2 for multifunctional stimulation, sensing, and therapy.

In summary, integrating 3D pseudocapacitive nanomaterials into optoelectronic biointerfaces shows excellent promise for wireless and electrical control of neurons. This study shows the successful integration of manganese dioxide nanoflowers into a flexible optoelectronic biointerface that can safely and efficiently stimulate neurons with low light intensity. The nanoflowers facilitated a high interfacial capacitance and photogenerated charge density, inducing reversible Faradaic reactions that did not cause any toxicity to hippocampal neurons in vitro. These findings suggest that 3D pseudocapacitive nanomaterials, such as MnO_2 nanoflowers, could be a reliable building block for future optoelectronic control of neurons. Furthermore, the ability of the optoelectronic biointerfaces to trigger repetitive and rapid firing of action potentials in response to light pulse trains can have significant applications in neuroprosthetics.

Chapter 4:
CONCLUSION

In this thesis, we explained the integration of MnO_2 nanoflowers into flexible optoelectronic biointerfaces to achieve efficient photostimulation of neurons. Valuable insights were gained regarding the nanoflowers' morphology, crystal structure, interfacial capacitance, charge injection properties, and their impact on neural stimulation with various characterization and testing techniques. For instance, scanning electron microscopy confirmed the successful deposition of MnO_2 nanoflowers on flexible substrates, revealing a specific 3D nanostructure composed of different-sized nanoflowers. This unique morphology increased the surface area significantly, which played a critical role in enhancing the electrochemical properties and overall performance of the biointerfaces.

The integration of MnO_2 nanoflowers leads to several findings that are significant to mention. Firstly, the nanoflowers exhibited lower impedance than previous studies utilizing RuO_2, indicating faster charge transfer characteristics. This impedance reduction was not only observed in comparison to other materials but also in comparison to the planar structure (seed layer) of MnO_2 itself, which further improved the electrical properties of the neural interfaces. Moreover, comparisons with existing literature showed the superior performance of MnO_2 nanoflowers integrated optoelectronic biointerfaces. The optimized MnO_2-based devices generated higher photocurrent and charge levels compared to recently reported organic optoelectronic biointerfaces, which suggests their potential for efficient and reliable photostimulation of neurons. Moreover, while MnO_2 nanoflowers displayed a high interfacial capacitance and photogenerated charge density due to reversible Faradaic reactions, they did not induce toxicity to hippocampal neurons. These findings support the hypothesis that 3D pseudocapacitive nanomaterials, such as MnO_2 nanoflowers, can be dependable building blocks for future optoelectronic control of neurons.

In summary, this thesis successfully demonstrated the integration of MnO2 nanoflowers into flexible optoelectronic biointerfaces, enabling efficient photostimulation of neurons, a high surface area, and improved electrochemical properties. Integration of a 3D supercapacitor led to reduced impedance, increased interfacial capacitance, and enhanced photogenerated charge density compared to previous studies and existing organic optoelectronic biointerfaces[10, 23, 29, 43, 86-91]. The research findings align with the objectives and hypotheses outlined in earlier chapters. The successful integration of MnO_2 nanoflowers may contribute significantly to future advancements in wireless and electrical control of neurons, with potential applications in neuroprosthetics and other biomedical fields. Further assessment of 3D supercapacitors and their combination with other functional devices holds promise for developing microscale, flexible, and multifunctional bioelectronic devices.

Overall, in the field of optoelectronic neural interfaces, this research contributes to the expanding cumulative knowledge and provides a foundation for future studies and innovations in neural stimulation, wearable devices, and bioengineering.

BIBLIOGRAPHY

[1] G. F. ERICKSON and A. Hsueh, "Stimulation of aromatase activity by follicle stimulating hormone in rat granulosa cells in vivo and in vitro," *Endocrinology,* vol. 102, no. 4, pp. 1275-1282, 1978.

[2] C. Magarinos-Ascone, J. Pazo, O. Macadar, and W. Buno, "High-frequency stimulation of the subthalamic nucleus silences subthalamic neurons: a possible cellular mechanism in Parkinson's disease," *Neuroscience,* vol. 115, no. 4, pp. 1109-1117, 2002.

[3] P. Anninos, N. Tsagas, R. Sandyk, and K. Derpapas, "Magnetic stimulation in the treatment of partial seizures," *International Journal of Neuroscience,* vol. 60, no. 2, pp. 141-171, 1991.

[4] S. I. Park *et al.*, "Soft, stretchable, fully implantable miniaturized optoelectronic systems for wireless optogenetics," *Nature biotechnology,* vol. 33, no. 12, pp. 1280-1286, 2015.

[5] A. M. Aravanis *et al.*, "An optical neural interface: in vivo control of rodent motor cortex with integrated fiberoptic and optogenetic technology," *Journal of neural engineering,* vol. 4, no. 3, p. S143, 2007.

[6] M. Han *et al.*, "Tissue-like optoelectronic neural interface enabled by PEDOT: PSS hydrogel for cardiac and neural stimulation," *Advanced Healthcare Materials,* vol. 11, no. 8, p. 2102160, 2022.

[7] R. A. Arkowitz and W. Wickner, "SecD and SecF are required for the proton electrochemical gradient stimulation of preprotein translocation," *The EMBO journal,* vol. 13, no. 4, pp. 954-963, 1994.

[8] D. Rand *et al.*, "Direct electrical neurostimulation with organic pigment photocapacitors," *Advanced Materials,* vol. 30, no. 25, p. 1707292, 2018.

[9] J. Bisquert, "Chemical capacitance of nanostructured semiconductors: its origin and significance for nanocomposite solar cells," *Physical Chemistry Chemical Physics,* vol. 5, no. 24, pp. 5360-5364, 2003.

[10] M. Han *et al.*, "Organic photovoltaic pseudocapacitors for neurostimulation," *ACS applied materials & interfaces,* vol. 12, no. 38, pp. 42997-43008, 2020.

[11] S. F. Cogan, "Neural stimulation and recording electrodes," *Annu. Rev. Biomed. Eng.,* vol. 10, pp. 275-309, 2008.

[12] B. E. Conway, V. Birss, and J. Wojtowicz, "The role and utilization of pseudocapacitance for energy storage by supercapacitors," *Journal of power sources,* vol. 66, no. 1-2, pp. 1-14, 1997.

[13] N. Zdolšek *et al.*, "Electrochemical investigation of ionic liquid-derived porous carbon materials for supercapacitors: pseudocapacitance versus electrical double layer," *Electrochimica Acta,* vol. 298, pp. 541-551, 2019.

[14] B. P. Bean, "The action potential in mammalian central neurons," *Nature Reviews Neuroscience,* vol. 8, no. 6, pp. 451-465, 2007.

[15] P. G. Wirsing, A. D. Habrom, T. M. Zehnder, S. Friedli, and M. Blatti, "Wireless micro current stimulation–an innovative electrical stimulation method for the treatment of patients with leg and diabetic foot ulcers," *International wound journal,* vol. 12, no. 6, pp. 693-698, 2015.

[16] H. Xu, L. Yin, C. Liu, X. Sheng, and N. Zhao, "Recent advances in biointegrated optoelectronic devices," *Advanced Materials,* vol. 30, no. 33, p. 1800156, 2018.

[17] S. Park, G. Loke, Y. Fink, and P. Anikeeva, "Flexible fiber-based optoelectronics for neural interfaces," *Chemical Society Reviews,* vol. 48, no. 6, pp. 1826-1852, 2019.
[18] K. Mathieson *et al.*, "Photovoltaic retinal prosthesis with high pixel density," *Nature photonics,* vol. 6, no. 6, pp. 391-397, 2012.
[19] E. Castagnola *et al.*, "PEDOT-CNT-coated low-impedance, ultra-flexible, and brain-conformable micro-ECoG arrays," *IEEE Transactions on Neural Systems and Rehabilitation Engineering,* vol. 23, no. 3, pp. 342-350, 2014.
[20] S. M. Won, E. Song, J. Zhao, J. Li, J. Rivnay, and J. A. Rogers, "Recent advances in materials, devices, and systems for neural interfaces," *Advanced Materials,* vol. 30, no. 30, p. 1800534, 2018.
[21] L. Kaya *et al.*, "MnO2 Nanoflower Integrated Optoelectronic Biointerfaces for Photostimulation of Neurons," *Advanced Science,* p. 2301854, 2023.
[22] J. M. Lee *et al.*, "All-tissue-like multifunctional optoelectronic mesh for deep-brain modulation and mapping," *Nano Letters,* vol. 21, no. 7, pp. 3184-3190, 2021.
[23] M. Silverå Ejneby *et al.*, "Chronic electrical stimulation of peripheral nerves via deep-red light transduced by an implanted organic photocapacitor," *Nature Biomedical Engineering,* vol. 6, no. 6, pp. 741-753, 2022.
[24] L. Ferlauto *et al.*, "Design and validation of a foldable and photovoltaic wide-field epiretinal prosthesis," *Nature communications,* vol. 9, no. 1, pp. 1-15, 2018.
[25] Y. Sun, T. Liu, Y. Kan, K. Gao, B. Tang, and Y. Li, "Flexible organic solar cells: progress and challenges," *Small Science,* vol. 1, no. 5, p. 2100001, 2021.
[26] K. Kostarelos, M. Vincent, C. Hebert, and J. A. Garrido, "Graphene in the design and engineering of next-generation neural interfaces," *Advanced Materials,* vol. 29, no. 42, p. 1700909, 2017.
[27] H. Park, A. R. Maple, and H. Lee, "Effects of Fractal Electrode Geometry in Charge Injection Capacity of TiN Microelectrodes," in *2020 42nd Annual International Conference of the IEEE Engineering in Medicine & Biology Society (EMBC)*, 2020: IEEE, pp. 3371-3374.
[28] L. Kergoat *et al.*, "PEDOT: PSS electrodes for acute experimental evaluation of vagus nerve stimulation on rodents," in *2018 40th Annual International Conference of the IEEE Engineering in Medicine and Biology Society (EMBC)*, 2018: IEEE, pp. 4760-4763.
[29] O. Karatum, H. N. Kaleli, G. O. Eren, A. Sahin, and S. Nizamoglu, "Electrical stimulation of neurons with quantum dots via near-infrared light," *Acs Nano,* vol. 16, no. 5, pp. 8233-8243, 2022.
[30] W. Zhang *et al.*, "Nitrogen-superdoped 3D graphene networks for high-performance supercapacitors," *Advanced Materials,* vol. 29, no. 36, p. 1701677, 2017.
[31] X. Qing *et al.*, "Facile synthesis of Co3O4 nanoflowers grown on Ni foam with superior electrochemical performance," *Electrochimica Acta,* vol. 56, no. 14, pp. 4985-4991, 2011.
[32] X. Yi, H. Sun, N. Robertson, and C. Kirk, "Nanoflower Ni (OH) 2 grown in situ on Ni foam for high-performance supercapacitor electrode materials," *Sustainable Energy & Fuels,* vol. 5, no. 20, pp. 5236-5246, 2021.

[33] Y. Wang, X. Li, N. Wang, X. Quan, and Y. Chen, "Controllable synthesis of ZnO nanoflowers and their morphology-dependent photocatalytic activities," *Separation and Purification Technology,* vol. 62, no. 3, pp. 727-732, 2008.
[34] M. Umadevi and A. J. Christy, "Synthesis, characterization and photocatalytic activity of CuO nanoflowers," *Spectrochimica Acta Part A: Molecular and Biomolecular Spectroscopy,* vol. 109, pp. 133-137, 2013.
[35] J.-Y. Kim, K.-H. Kim, H.-K. Kim, S.-H. Park, K. Y. Chung, and K.-B. Kim, "Nanosheet-assembled 3D nanoflowers of ruthenium oxide with superior rate performance for supercapacitor applications," *RSC Advances,* vol. 4, no. 31, pp. 16115-16120, 2014.
[36] Q. Z. Zhang, D. Zhang, Z. C. Miao, X. L. Zhang, and S. L. Chou, "Research progress in MnO2–carbon based supercapacitor electrode materials," *Small,* vol. 14, no. 24, p. 1702883, 2018.
[37] S. Devaraj and N. Munichandraiah, "High capacitance of electrodeposited MnO2 by the effect of a surface-active agent," *Electrochemical and Solid-State Letters,* vol. 8, no. 7, p. A373, 2005.
[38] G. Zhu, H. Li, L. Deng, and Z.-H. Liu, "Low-temperature synthesis of δ-MnO2 with large surface area and its capacitance," *Materials Letters,* vol. 64, no. 16, pp. 1763-1765, 2010.
[39] G.-S. Tran, T.-G. Vo, and C.-Y. Chiang, "Earth-abundant manganese oxide nanoneedle as highly efficient electrocatalyst for selective glycerol electro-oxidation to dihydroxyacetone," *Journal of Catalysis,* vol. 404, pp. 139-148, 2021.
[40] A. Das, L. Sukla, N. Pradhan, and S. Nayak, "Manganese biomining: a review," *Bioresource Technology,* vol. 102, no. 16, pp. 7381-7387, 2011.
[41] Y.-Z. Wu, Y. Ding, T. Hayat, A. Alsaedi, and S.-Y. Dai, "Enlarged working potential window for MnO2 supercapacitors with neutral aqueous electrolytes," *Applied Surface Science,* vol. 459, pp. 430-437, 2018.
[42] J. Dykstra, K. Keesman, P. Biesheuvel, and A. Van der Wal, "Theory of pH changes in water desalination by capacitive deionization," *Water research,* vol. 119, pp. 178-186, 2017.
[43] O. Karatum, E. Yildiz, H. N. Kaleli, A. Sahin, B. Ulgut, and S. Nizamoglu, "RuO2 Supercapacitor Enables Flexible, Safe, and Efficient Optoelectronic Neural Interface," *Advanced Functional Materials,* vol. 32, no. 31, p. 2109365, 2022.
[44] V. A. Pavlov and K. J. Tracey, "Bioelectronic medicine: preclinical insights and clinical advances," *Neuron,* 2022.
[45] R. Plonsey, R. C. Barr, and A. Bioelectricity, *Quantitative Approach*. Springer, 2007.
[46] M. Han, O. Karatum, and S. Nizamoglu, "Optoelectronic Neural Interfaces Based on Quantum Dots," *ACS Applied Materials & Interfaces,* vol. 14, no. 18, pp. 20468-20490, 2022/05/11 2022, doi: 10.1021/acsami.1c25009.
[47] S. M. Won, E. Song, J. T. Reeder, and J. A. Rogers, "Emerging modalities and implantable technologies for neuromodulation," *Cell,* vol. 181, no. 1, pp. 115-135, 2020.
[48] B. Park *et al.*, "Cuticular pad–inspired selective frequency damper for nearly dynamic noise–free bioelectronics," *Science,* vol. 376, no. 6593, pp. 624-629, 2022.

[49] B. Joy, Y. Cai, D. C. Bono, and D. Sarkar, "Cell Rover—a miniaturized magnetostrictive antenna for wireless operation inside living cells," *Nature Communications,* vol. 13, no. 1, p. 5210, 2022.
[50] Y. Jiang *et al.*, "Rational design of silicon structures for optically controlled multiscale biointerfaces," *Nature biomedical engineering,* vol. 2, no. 7, pp. 508-521, 2018.
[51] R. Parameswaran *et al.*, "Optical stimulation of cardiac cells with a polymer-supported silicon nanowire matrix," *Proceedings of the National Academy of Sciences,* vol. 116, no. 2, pp. 413-421, 2019.
[52] D. Palanker, Y. Le Mer, S. Mohand-Said, and J.-A. Sahel, "Simultaneous perception of prosthetic and natural vision in AMD patients," *Nature communications,* vol. 13, no. 1, p. 513, 2022.
[53] S. P. Lacour, G. Courtine, and J. Guck, "Materials and technologies for soft implantable neuroprostheses," *Nature Reviews Materials,* vol. 1, no. 10, pp. 1-14, 2016.
[54] L. Ferlauto *et al.*, "Design and validation of a foldable and photovoltaic wide-field epiretinal prosthesis," *Nature communications,* vol. 9, no. 1, p. 992, 2018.
[55] M. Jakešová *et al.*, "Optoelectronic control of single cells using organic photocapacitors," *Science advances,* vol. 5, no. 4, p. eaav5265, 2019.
[56] N. A. L. Chenais, M. J. I. Airaghi Leccardi, and D. Ghezzi, "Photovoltaic retinal prosthesis restores high-resolution responses to single-pixel stimulation in blind retinas," *Communications Materials,* vol. 2, no. 1, p. 28, 2021.
[57] K. Q. Ding, "Cyclic Voltammetrically-Prepared MnO2 Coated on an ITO Glass Substrate," *Journal of the Chinese Chemical Society,* vol. 56, no. 1, pp. 175-181, 2009.
[58] A. Aref and Y. Tang, "Chemical bath deposition synthesis and electrochemical properties of MnO2 thin film: Effect of deposition time and bath temperature," *Materials Science-Poland,* vol. 32, no. 4, pp. 555-564, 2014.
[59] O. Sadak, W. Wang, J. Guan, A. K. Sundramoorthy, and S. Gunasekaran, "MnO2 nanoflowers deposited on graphene paper as electrode materials for supercapacitors," *ACS Applied Nano Materials,* vol. 2, no. 7, pp. 4386-4394, 2019.
[60] H. Kang *et al.*, "Preparation of MOF/polypyrrole and flower-like MnO2 electrodes by electrodeposition: High-performance materials for hybrid capacitive deionization defluorination," *Water Research,* vol. 229, p. 119441, 2023.
[61] Z. Li, T. Feng, P. Zhou, R. Zhang, and G. Liu, "Growth of Flower-like MnO2 on Porous ZIF-67 for Achieving Enhanced Supercapacitive Properties," *Energy & Fuels,* vol. 36, no. 23, pp. 14490-14499, 2022.
[62] I. I. Misnon, R. Abd Aziz, N. K. M. Zain, B. Vidhyadharan, S. G. Krishnan, and R. Jose, "High performance MnO2 nanoflower electrode and the relationship between solvated ion size and specific capacitance in highly conductive electrolytes," *Materials Research Bulletin,* vol. 57, pp. 221-230, 2014.
[63] M. Toupin, T. Brousse, and D. Bélanger, "Charge storage mechanism of MnO2 electrode used in aqueous electrochemical capacitor," *Chemistry of Materials,* vol. 16, no. 16, pp. 3184-3190, 2004.
[64] W. Li *et al.*, "MnO2 nanoflower arrays with high rate capability for flexible supercapacitors," *ChemElectroChem,* vol. 1, no. 6, pp. 1003-1008, 2014.

[65] Z. Li, Y. Mi, X. Liu, S. Liu, S. Yang, and J. Wang, "Flexible graphene/MnO 2 composite papers for supercapacitor electrodes," *Journal of Materials Chemistry,* vol. 21, no. 38, pp. 14706-14711, 2011.
[66] E. Beyreuther, S. Grafström, L. M. Eng, C. Thiele, and K. Dörr, "XPS investigation of Mn valence in lanthanum manganite thin films under variation of oxygen content," *Physical Review B,* vol. 73, no. 15, p. 155425, 2006.
[67] S. F. Cogan, "Neural stimulation and recording electrodes," *Annual review of biomedical engineering,* vol. 10, no. 1, pp. 275-309, 2008.
[68] A. Corna, T. Herrmann, and G. Zeck, "Electrode-size dependent thresholds in subretinal neuroprosthetic stimulation," *Journal of neural engineering,* vol. 15, no. 4, p. 045003, 2018.
[69] W. Wei, X. Cui, W. Chen, and D. G. Ivey, "Manganese oxide-based materials as electrochemical supercapacitor electrodes," *Chemical society reviews,* vol. 40, no. 3, pp. 1697-1721, 2011.
[70] M. Ciocca *et al.*, "A Polymer Bio–Photoelectrolytic Platform for Electrical Signal Measurement and for Light Modulation of Ion Fluxes and Proliferation in a Neuroblastoma Cell Line," *Advanced NanoBiomed Research,* p. 2200127, 2022.
[71] H. J. Kaplan and J. P. F. de Castro, "Retinal regeneration and stem cell therapy in retinitis pigmentosa," *Taiwan Journal of Ophthalmology,* vol. 2, no. 2, pp. 41-44, 2012.
[72] M. L. DiFrancesco *et al.*, "A hybrid P3HT-graphene interface for efficient photostimulation of neurons," *Carbon,* vol. 162, pp. 308-317, 2020.
[73] I. Schoen and P. Fromherz, "The mechanism of extracellular stimulation of nerve cells on an electrolyte-oxide-semiconductor capacitor," *Biophysical journal,* vol. 92, no. 3, pp. 1096-1111, 2007.
[74] Y. Jiang *et al.*, "Neural stimulation in vitro and in vivo by photoacoustic nanotransducers," *Matter,* vol. 4, no. 2, pp. 654-674, 2021.
[75] X. Wu *et al.*, "Tether-free photothermal deep-brain stimulation in freely behaving mice via wide-field illumination in the near-infrared-II window," *Nature Biomedical Engineering,* vol. 6, no. 6, pp. 754-770, 2022.
[76] Q. Xiong, H. V. Oviedo, L. C. Trotman, and A. M. Zador, "PTEN regulation of local and long-range connections in mouse auditory cortex," *Journal of Neuroscience,* vol. 32, no. 5, pp. 1643-1652, 2012.
[77] E. S. Boyden, F. Zhang, E. Bamberg, G. Nagel, and K. Deisseroth, "Millisecond-timescale, genetically targeted optical control of neural activity," *Nature neuroscience,* vol. 8, no. 9, pp. 1263-1268, 2005.
[78] Y. Yang, M. DeWeese, G. Otazu, and A. Zador, "Millisecond-scale differences in neural activity in auditory cortex can drive decisions," *Nature Precedings,* pp. 1-1, 2008.
[79] J. A. Garcia-Lazaro, L. A. Belliveau, and N. A. Lesica, "Independent population coding of speech with sub-millisecond precision," *Journal of Neuroscience,* vol. 33, no. 49, pp. 19362-19372, 2013.
[80] A. Mohanty *et al.*, "Reconfigurable nanophotonic silicon probes for sub-millisecond deep-brain optical stimulation," *Nature biomedical engineering,* vol. 4, no. 2, pp. 223-231, 2020.
[81] O. A. Shemesh *et al.*, "Temporally precise single-cell-resolution optogenetics," *Nature neuroscience,* vol. 20, no. 12, pp. 1796-1806, 2017.

[82] H. Kim and B. N. Popov, "Synthesis and characterization of MnO2-based mixed oxides as supercapacitors," *Journal of the Electrochemical Society,* vol. 150, no. 3, p. D56, 2003.
[83] Y. Li and H. Xie, "Mechanochemical-synthesized Al-doped manganese dioxides for electrochemical supercapacitors," *Ionics,* vol. 16, pp. 21-25, 2010.
[84] X. Pang, Z.-Q. MA, and L. Zuo, "Sn doped MnO2 electrode material for supercapacitors," *Acta Physico-Chimica Sinica,* vol. 25, no. 12, pp. 2433-2437, 2009.
[85] J. J. Pancrazio *et al.*, "Thinking small: Progress on microscale neurostimulation technology," *Neuromodulation: Technology at the Neural Interface,* vol. 20, no. 8, pp. 745-752, 2017.
[86] O. Karatum *et al.*, "Nanoengineering InP quantum dot-based photoactive biointerfaces for optical control of neurons," *Frontiers in Neuroscience,* vol. 15, p. 652608, 2021.
[87] M. Han, H. Bahmani Jalali, E. Yildiz, M. H. Qureshi, A. Şahin, and S. Nizamoglu, "Photovoltaic neurointerface based on aluminum antimonide nanocrystals," *Communications Materials,* vol. 2, no. 1, p. 19, 2021.
[88] O. Karatum *et al.*, "Quantum dot and electron acceptor nano-heterojunction for photo-induced capacitive charge-transfer," *Scientific reports,* vol. 11, no. 1, p. 2460, 2021.
[89] M. Silverå Ejneby *et al.*, "Extracellular photovoltage clamp using conducting polymer-modified organic photocapacitors," *Advanced Materials Technologies,* vol. 5, no. 3, p. 1900860, 2020.
[90] O. S. Abdullaeva *et al.*, "Organic photovoltaic sensors for photocapacitive stimulation of voltage-gated ion channels in neuroblastoma cells," *Advanced Functional Materials,* vol. 29, no. 21, p. 1805177, 2019.
[91] R. Melikov *et al.*, "Plasmon-coupled photocapacitor neuromodulators," *ACS applied materials & interfaces,* vol. 12, no. 32, pp. 35940-35949, 2020.
[92] D. Ghezzi *et al.*, "A polymer optoelectronic interface restores light sensitivity in blind rat retinas," *Nature Photonics,* vol. 7, no. 5, pp. 400-406, 2013.
[93] H. Bahmani Jalali *et al.*, "Biocompatible quantum funnels for neural photostimulation," *Nano letters,* vol. 19, no. 9, pp. 5975-5981, 2019.
[94] M. J. I. Airaghi Leccardi, N. A. L. Chenais, L. Ferlauto, M. Kawecki, E. G. Zollinger, and D. Ghezzi, "Photovoltaic organic interface for neuronal stimulation in the near-infrared," *Communications Materials,* vol. 1, no. 1, p. 21, 2020.
[95] S. Chattopadhyay *et al.*, "Toxicity of cobalt oxide nanoparticles to normal cells; an in vitro and in vivo study," *Chemico-biological interactions,* vol. 226, pp. 58-71, 2015.
[96] R. Liang *et al.*, "Transition metal oxide electrode materials for supercapacitors: a review of recent developments," *Nanomaterials,* vol. 11, no. 5, p. 1248, 2021.
[97] L. Yang *et al.*, "A biodegradable hybrid inorganic nanoscaffold for advanced stem cell therapy," *Nature communications,* vol. 9, no. 1, p. 3147, 2018.
[98] Y. Yang *et al.*, "MnO2 Nanoflowers Induce Immunogenic Cell Death under Nutrient Deprivation: Enabling an Orchestrated Cancer Starvation-Immunotherapy," *Advanced Science,* vol. 8, no. 4, p. 2002667, 2021.
[99] M. Wu *et al.*, "Manganese dioxide nanosheets: from preparation to biomedical applications," *International journal of nanomedicine,* pp. 4781-4800, 2019.